

A global view of stratospheric gravity wave hotspots located with Atmospheric Infrared Sounder observations

L. Hoffmann,¹ X. Xue,^{2,3} and M. J. Alexander⁴

Received 6 August 2012; revised 28 November 2012; accepted 29 November 2012; published 25 January 2013.

[1] The main aim of this study is to find and classify hotspots of stratospheric gravity waves on a global scale. The analysis is based on a 9 year record (2003 to 2011) of radiance measurements by the Atmospheric Infrared Sounder (AIRS) aboard NASA's Aqua satellite. We detect gravity waves based on 4.3 μm brightness temperature variances. Our method focuses on peak events, i.e., strong gravity wave events for which the local variance considerably exceeds background levels. We estimate the occurrence frequencies of these peak events for different seasons and time of day and use the results to find local maxima or "hotspots." In addition, we use AIRS radiances at 8.1 μm to simultaneously detect convective events, including deep convection in the tropics and mesoscale convective systems at middle latitudes. We classify the gravity wave sources based on seasonal occurrence frequencies for convection, but also by means of time series analyses and topographic data. Our study reproduces well-known hotspots of gravity waves, e.g., the Andes and the Antarctic Peninsula. However, the high horizontal resolution of the AIRS observations also allows us to locate numerous mesoscale hotspots, which are partly unknown or poorly studied so far. Most of these mesoscale hotspots are found near orographic features like mountain ranges, coasts, lakes, deserts, or isolated islands. This study will help to select promising regions and seasons for future case studies of gravity waves.

Citation: Hoffmann, L., X. Xue, and M. J. Alexander (2013), A global view of stratospheric gravity wave hotspots located with Atmospheric Infrared Sounder observations, *J. Geophys. Res. Atmos.*, 118, 416–434, doi:10.1029/2012JD018658.

1. Introduction

[2] Gravity waves transport energy and momentum, contribute to turbulence and mixing, and influence the mean circulation and thermal structure of the middle atmosphere [Lindzen, 1981; Holton, 1982, 1983; Becker and McLandress, 2009]. The most prominent sources of gravity waves are orographic generation [Smith, 1985; Durran and Klemp, 1987; Nastrom and Fritts, 1992; Dörnbrack et al., 1999] and convection [Pfister et al., 1986; Tsuda et al., 1994; Alexander and Pfister, 1995; Vincent and Alexander, 2000]. Other sources that are important, at least for certain meteorological conditions, are wind shear, adjustment of

unbalanced flows near jet streams and frontal systems, body forcing accompanying localized wave dissipation, and wave-wave interaction [Fritts and Alexander, 2003; Vadas et al., 2003; Wu and Zhang, 2004]. A large number of observational and theoretical studies has advanced understanding of different aspects of gravity waves, including the characteristics of the wave sources and the evolution of the wave spectrum with altitude-dependent wind and stability variations. However, further research is still necessary.

[3] Satellite instruments offer an excellent opportunity for global studies of the characteristics of gravity waves. The main advantage of limb and occultation experiments is good vertical resolution and sensitivity to gravity waves with short vertical wavelengths. However, a disadvantage of current limb sounders is the limited horizontal resolution and reduced sensitivity to short horizontal wavelengths [Preusse et al., 2008, 2009]. In contrast, nadir instruments are typically limited to observations of gravity waves with longer vertical wavelengths, but they provide better horizontal resolution.

[4] This study focuses on nadir observations made by the Atmospheric Infrared Sounder (AIRS) aboard NASA's Aqua satellite. We analyze radiance measurements, because these are provided at high horizontal resolution for each satellite footprint. AIRS operational temperature retrievals have degraded horizontal resolution as 3×3 footprints are combined within a cloud-clearing procedure. AIRS observations

¹Forschungszentrum Jülich, Jülich Supercomputing Centre, Wilhelm-Johnen-Strasse 52425, Jülich, Germany.

²CAS Key Laboratory of Geospace Environment, Department of Geophysics & Planetary Sciences, University of Science and Technology of China, Hefei, Anhui, China.

³Mengcheng National Geophysical Observatory, School of Earth and Space Sciences, University of Science and Technology of China, Hefei, Anhui, China.

⁴NorthWest Research Associates, Inc., Colorado Research Associates Division, Boulder, Colorado, USA.

Corresponding author: L. Hoffmann, Forschungszentrum Jülich, Jülich Supercomputing Centre, Wilhelm-Johnen-Strasse, 52425 Jülich, Germany. (l.hoffmann@fz-juelich.de)

©2012. American Geophysical Union. All Rights Reserved.
2169-897X/13/2012JD018658

were successfully exploited for gravity wave research by *Wu et al.* [2006], *Alexander and Teitelbaum* [2007], *Eckermann et al.* [2007], *Alexander et al.* [2009a], *Hecht et al.* [2009], *Hoffmann and Alexander*, 2009, *Kim et al.* [2009], *Grimsdell et al.* [2010], *Hoffmann and Alexander* [2010], *Alexander and Teitelbaum* [2011], and *Gong et al.* [2012].

[5] Radiance measurements from infrared nadir sounders can also be used to detect the presence of high cold clouds related to deep convection. *Aumann et al.* [2006, 2007, 2008, 2011] used AIRS observations for detailed statistical analyses of deep convective clouds in the tropics. For gravity wave research, it is potentially promising that AIRS data can be used to simultaneously detect stratospheric gravity waves and convection in the same footprint. *Hoffmann and Alexander* [2010] used AIRS data to locate mesoscale convective systems during the North American thunderstorm season and related simultaneous observations of stratospheric gravity waves to these events.

[6] The potential of AIRS data that became evident in the study of *Hoffmann and Alexander* [2010] motivated us to assess the distributions of gravity waves on a global scale. We were particularly interested in the occurrence of gravity wave peak events, i.e., strong gravity wave events for which the local brightness temperature variances significantly exceed background levels. We wanted to know where and how often these peak events occur and if the observed waves could be related to different source mechanisms like orography and convection. For this study, we had to optimize our detection methods for gravity waves and convection to be applicable on a global scale. We applied the optimized detection methods to estimate seasonal peak event frequencies of stratospheric gravity waves and occurrence frequencies of convection during daytime and nighttime.

[7] Despite being limited in vertical resolution, the AIRS data are well suited to detect stratospheric gravity waves. Major advantages of the AIRS data are the good horizontal resolution and the long time series of observations. The measurements allowed us to locate the hotspots of gravity wave peak events with unprecedented horizontal resolution ($0.5^\circ \times 0.5^\circ$). Substantial progress is related to the amount of observational data that were analyzed in this study. The analysis covers nine years (2003 to 2011) of AIRS observations, i.e., nearly 9.6×10^9 individual satellite footprints, on a global scale. The long time series allowed us to calculate statistics that cover interannual atmospheric variability, e.g., the variability due to the quasi-biennial oscillation.

[8] In section 2 of this paper, we provide a brief description of the AIRS instrument, including its measurement geometry, data coverage, and some examples of radiance measurements. In section 3 we describe the detection method for stratospheric gravity waves. We present seasonal means of gravity wave peak event frequencies during both daytime and nighttime. Section 4 introduces the detection method for convection. We discuss seasonal means of occurrence frequencies of convection and analyze correlations between gravity waves and convection based on local, daily time series. Section 5 presents the gravity wave hotspots for different seasons and time of day. This includes references to previous case studies related to the individual hotspots, as far as these were found. Finally, conclusions and outlook are presented in section 6.

2. The AIRS Instrument

2.1. Measurement Geometry and Data Coverage

[9] On 4 May 2002, NASA launched the Aqua satellite [*Parkinson*, 2003] aboard a Delta II rocket from Vandenberg Air Force Base, California, United States. The Aqua mission is part of NASA's Earth Observing System. Aqua is the first satellite in the "A-Train" constellation of satellites. Aqua operates at 705 km altitude in a Sun-synchronous polar orbit with 98° inclination and 99 min period. Global coverage is achieved during 14.5 orbits per day. Six instruments aboard Aqua monitor the global state of the Earth's atmosphere.

[10] The AIRS [*Aumann et al.*, 2003] measures the thermal emissions of atmospheric constituents in the nadir and sublimb observation geometry. AIRS applies a rotating mirror to carry out sublimb scans in the across-track direction. A scan consists of 90 individual footprints and covers an across-track distance of 1765 km on the ground or $\pm 48.95^\circ$ in scan angle. A scan is measured in 2.667 s. The along-track distance between two scans is 18 km. The AIRS measurements are gathered in "granules." Each granule covers six minutes of measurement time, i.e., 135 scans or 12,150 footprints. The along-track size of a granule is 2430 km. The AIRS aperture is 1.1° , corresponding to a spatial resolution of 13.5 km at nadir and $41 \text{ km} \times 21.4 \text{ km}$ at the scan extremes.

[11] The AIRS has provided nearly continuous measurement coverage since September 2002. During the years 2003 to 2011, i.e., during the time period analyzed in this paper, measurement dropouts of more than a day occur only from 29 October to 18 November 2003 and from 9 to 26 January 2011. During a single day, AIRS measures about 2.9 million radiance spectra globally. For some of the statistical analyses presented in this study, the AIRS data are binned into a $0.5^\circ \times 0.5^\circ$ longitude-latitude grid. Figure 1a presents the data coverage for these grid boxes as a function of latitude. In the latitude range from 82°S to 82°N there are typically 10 to 16 footprints in each grid box per day.

[12] We separate daytime and nighttime observations based on the local time of the AIRS footprints. If the local time of a footprint is in between 6 A.M. and 6 P.M., it is considered to be a daytime observation; otherwise, it is considered a nighttime observation. Figure 1b presents the local time for the nadir and outermost measurement tracks as a function of latitude. It illustrates that a clear separation of daytime and nighttime data is only possible at low and middle latitudes. For the nadir track the equatorial crossing occurs at 1:30 P.M. local time (ascending orbit) and 1:30 A.M. local time (descending orbit). Within each scan the local time varies by ± 30 min at the equator. The variation stays within ± 70 min up to $\pm 60^\circ$ latitude. A quick transition between daytime and nighttime occurs at higher latitudes.

2.2. Radiance Measurements

[13] The AIRS radiance measurements cover the wavelength ranges 3.74 to 4.61 μm , 6.20 to 8.22 μm , and 8.8 to 15.4 μm . A diffraction grating disperses the scene radiance on 17 linear arrays of HgCdTe-detectors, providing a total of 2378 radiance channels. The nominal resolving power of the hyperspectral infrared radiometer is $\lambda/\Delta\lambda = 1200$. The radiances have an absolute accuracy of 3% (at 190

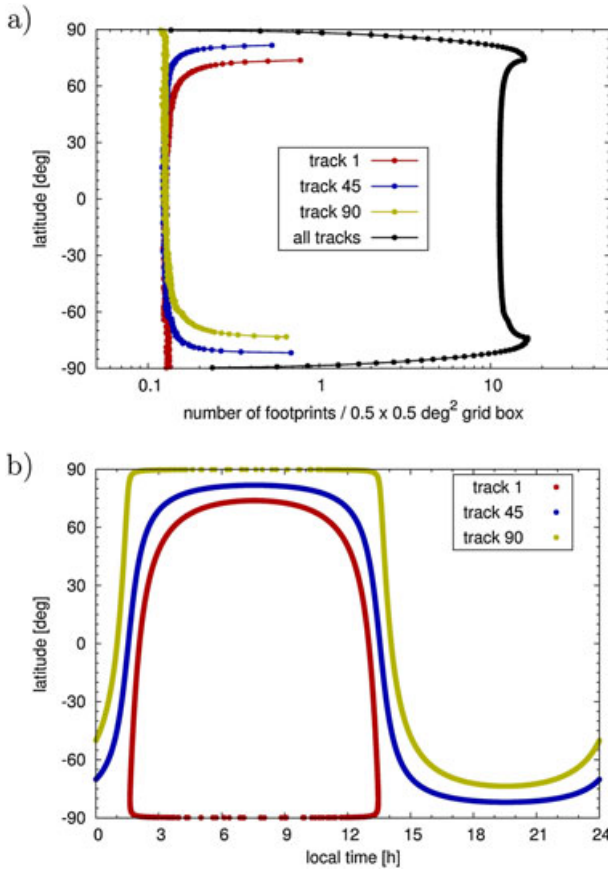


Figure 1. AIRS orbit data for 1 January 2003. Shown are (a) data coverage and (b) local time versus latitude for the nadir measurement track (track 45), the outermost scans of the swath (track 1 and 90), and all tracks. The satellite orbit is actively maintained to control its repeat cycle, i.e., data shown here are representative for the years 2003 to 2011.

to 330 K scene radiance) and a relative accuracy of 0.2 K (at 250 K). *Aumann et al.* [2000, 2003] described the processing of instrument raw data into calibrated radiance spectra (Level-1B data). The analyses presented in this paper are based on consolidated Level-1B data products (version 5.x) made freely available by NASA.

[14] As an example, Figure 2 shows two radiance spectra measured at tropical latitudes. One spectrum was measured in the presence of deep convective clouds while the other one was measured in a cloud-free scene. A substantial difference of 115 K in brightness temperature is evident at 8.1 μm . In the case of the deep convective cloud the brightness temperature is low because cold temperatures (~ 185 K) at the cloud top are sensed. In the cloud-free scene much warmer surface temperatures (~ 300 K) are measured. This difference allows us to use the AIRS radiance measurements at 8.1 μm to detect the presence of convection. At 4.3 μm the atmosphere becomes optically thick in the stratosphere due to strong absorption bands of CO_2 . Tropospheric emissions from clouds or interfering species, e.g., water vapor, do not influence these measurements. The observed variability in radiance is primarily due to changes in stratospheric temperature. AIRS radiance measurements at 4.3 μm are used to detect gravity waves.

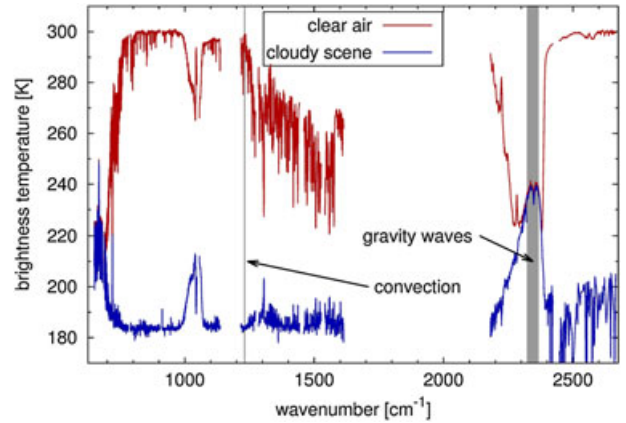


Figure 2. Examples of clear air and cloudy radiance spectra measured by AIRS on 12 January 2003, 16:45 UTC near 128.9°E, 19.4°S and 130.6°E, 12.2°S, respectively. Gray shaded areas at 4.3 μm (2323 to 2367 cm^{-1}) and 8.1 μm (1231 cm^{-1}) indicate spectral regions used to detect gravity waves and convection.

3. Gravity Wave Peak Events

3.1. Detection of Stratospheric Gravity Waves

[15] Previous studies showed that stratospheric gravity waves can be detected directly in AIRS radiance measurements [e.g., *Alexander and Teitelbaum*, 2007; *Hoffmann and Alexander*, 2010; *Gong et al.*, 2012]. Our analysis is based on average brightness temperatures from 42 AIRS channels in the 4.3 μm CO_2 fundamental band (2322.6 to 2345.9 cm^{-1} and 2352.5 to 2366.9 cm^{-1} , AIRS channel numbers 2040 to 2065 and 2072 to 2087). This channel selection is the same as that used by *Hoffmann and Alexander* [2010]. We selected the channels based on an analysis of temperature weighting functions. All the chosen channels become optically thick at stratospheric height levels. They have similar weighting functions in terms of peak height, which is in between 30 and 40 km, and full width at half maximum, which is about 25 km. Below 18 to 20 km the sensitivity of the weighting functions drops below 1% of the maximum, i.e., these channels are not affected by surface emissions, tropospheric clouds, or reflected sunlight.

[16] Information on stratospheric gravity waves can also be deduced from AIRS channels covering the 15 μm CO_2 fundamental band. However, most of these channels are sensitive to lower altitudes. The number of channels at 15 μm , which are sensitive to temperature perturbations in the middle and upper stratosphere, is rather limited compared with the 4.3 μm band [*Hoffmann and Alexander*, 2009]. Using the 4.3 μm band allows us to combine a large number of channels and reduce the measurement noise. This improves the sensitivity to gravity waves with short vertical wavelengths. Although the weighting functions at 4.3 μm are rather broad (~ 25 km full width at half maximum), the detection method presented here is sensitive to vertical wavelengths as short as ~ 15 km in many cases. This is illustrated in more detail in section 3.2.

[17] We calculate brightness temperature perturbations as differences from a fourth-order polynomial fit for each scan. First, this removes the increase in radiance with increasing

scan angle related to elongated atmospheric paths in the sublimb direction. Second, it removes slowly varying atmospheric background signals, e.g., due to planetary waves. The same method for background estimation was previously used by *Alexander and Barnett* [2007] and *Hoffmann and Alexander* [2010]. A similar approach of background estimation was developed by *Wu* [2004] for analysis of the Advanced Microwave Sounding Unit-A radiances. In contrast to our approach, *Wu* [2004] uses third-order polynomial fits for each half of the Advanced Microwave Sounding Unit-A scan. These fits are constrained by data from 15 footprints each. The fourth-order fit applied here is constrained by 90 footprints for the full scan. A visual inspection of the fit results did not show any problems with spurious oscillations. The fit results are also identical to the background removal method applied by *Eckermann et al.* [2006] for the short horizontal wavelength waves of interest.

[18] We identify stratospheric gravity waves based on local variances that are calculated from the brightness temperature perturbations. Following the approach of *Hoffmann and Alexander* [2010], we compute the local variances for each footprint based on data of the surrounding footprints within 100 km radius. In general, the observed variances (σ^2) have two main components, $\sigma^2 = \sigma_{\text{GW}}^2 + \sigma_N^2$, the contributions due to gravity waves (σ_{GW}^2) and instrument noise (σ_N^2). A variance filter is a direct and simple way to distinguish gravity wave disturbances from instrument noise. *Hoffmann and*

Alexander [2010] used such a filter to detect large amplitude gravity waves in midlatitude summer conditions when σ^2 exceeded a variance threshold $\sigma_T^2 = 0.05 \text{ K}^2$, which is about a factor 50 higher than $\sigma_N^2 = (0.2 \text{ K}/\sqrt{42})^2 \approx 0.001 \text{ K}^2$. However, to investigate gravity waves on a global scale for different atmospheric conditions and to focus on peak events, the selection of thresholds had to be revisited.

[19] Figure 3 shows brightness temperature variance versus latitude for three scan angles of ascending and descending orbits in September (Figures 3a and 3c) and December (Figures 3b and 3d) for the year 2003. Each point represents the zonal mean of the brightness temperature variance on a single day in 0.5° latitudinal bins. The variances in each scan angle show similar characteristics with respect to their latitudinal and seasonal variations. At equinox the brightness temperature variances are small at low latitudes and large at high latitudes (Figures 3a and 3c). The largest variability is found in the spring hemisphere. At solstice the largest brightness temperature variances appear in the winter hemisphere in the polar regions (Figures 3b and 3d). The lowest values are found in the summer hemisphere. At lower latitudes a secondary maximum is observed in the summer hemisphere.

[20] These general patterns can be explained by stratospheric wind filtering and the visibility of gravity waves to the instrument. Figure 4 shows zonal mean zonal winds at 10 hPa for different months from reanalysis of the National Center for Atmospheric Research (NCAR) and

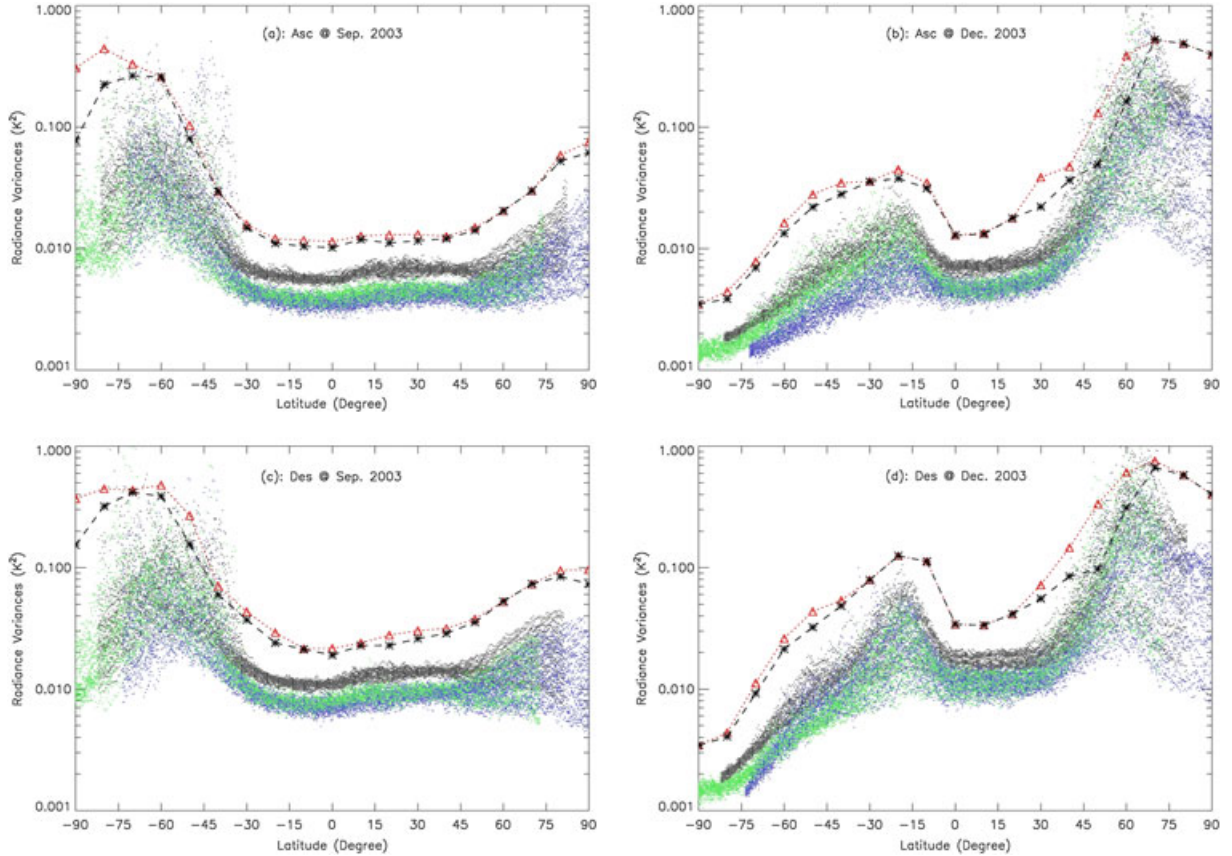


Figure 3. Radiance variances versus latitude for three scan angles (nadir, black dots; outermost tracks, green and blue dots). (a, b) Ascending orbits and (c, d) descending orbits. September 2003 is shown in the left column and December 2003 in the right. Black stars represent the variance thresholds for each data set. Red triangles represent variance thresholds calculated from 5 years of variance data.

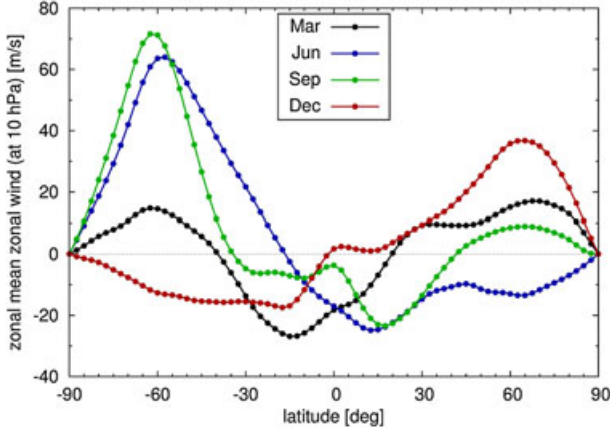


Figure 4. Zonal mean zonal winds at 10 hPa from NCAR/NCEP reanalysis for different months. Averages are computed based on 5 years of data (2003 to 2007).

National Centers for Environmental Prediction (NCEP) [Kalnay *et al.*, 1996]. Considering that the gravity wave vertical wavelength is in a broad sense proportional to the wind, this plot illustrates at which latitudes gravity waves with long wavelengths preferably propagate into the stratosphere. Because the AIRS observations are limited to long vertical wavelengths, Figure 4 provides a simple proxy for visibility. The latitudinal characteristics found in the zonal mean zonal wind correlate with the observed brightness temperature variances in Figure 3.

[21] Figure 3 shows strong variations of the brightness temperature variances with latitude and season, which we have to consider in the selection of detection thresholds to focus on peak events. Concerning daytime and nighttime differences, it is found that the variances of the descending orbits are larger than those of the ascending orbits. The mean difference is about 0.01 K^2 . Therefore, we separate daytime and nighttime observations in the analysis. Figure 3 also suggests that the variances for nadir are slightly higher than those for the outermost scan angles. This can be explained by the fact that the calculation of the variances for the outer tracks is based on fewer footprints than for the inner tracks. The individual variances are based on 50 to 130 AIRS footprints each, with the maximum number being used in the nadir direction and the minimum number being used for the scan extremes. However, this difference in scan angle is not taken into account any further in this study. Overall, we consider detection thresholds, which vary with respect to latitude, month, and time of day.

[22] To determine the thresholds, we first collected all brightness temperature variance data from AIRS scan angles with footprints located in a longitudinal slice between 160°W and 180°W . This region over the central Pacific is primarily ocean and convective activity is less frequent. It is a relatively quiet area in terms of gravity wave activity. Nearly 2.5 million brightness temperature variance values were gathered for this region every month. We sorted the data into 10° latitudinal bins, $\theta = 0, \pm 10^\circ, \dots, \pm 90^\circ$ and $\theta_i \in [\theta - 5^\circ, \theta + 5^\circ]$. Next, an initial variance threshold was calculated for each latitude band,

$$\sigma_T^2(\theta) = \sigma^2(\theta) + 5 \times \sqrt{\frac{1}{N-1} \sum_{i=1}^N [\sigma^2(\theta_i) - \sigma^2(\theta)]^2}, \quad (1)$$

where the mean variance is defined by

$$\sigma^2(\theta) = \frac{1}{N} \sum_{i=1}^N \sigma^2(\theta_i) \quad (2)$$

and N refers to the number of variance values per latitude band. Brightness temperature variances larger than this initial threshold were then excluded from the data set. The final variance thresholds were calculated by applying equations (1) and (2) again.

[23] The examples presented so far use data from only one year, 2003. Our final thresholds are computed using the maxima from 5 years of data, 2003 to 2007. Although interannual variability is not strong, the use of multiple years does raise the thresholds slightly (as can be seen by comparing the red triangles to the black stars in Figure 3). Figure 5 shows the final detection thresholds for March, June, September, and December for ascending and descending orbits. We find the same latitudinal variations for the ascending and descending orbits, but with different absolute values of the variance thresholds. Changes in the thresholds in the equatorial region

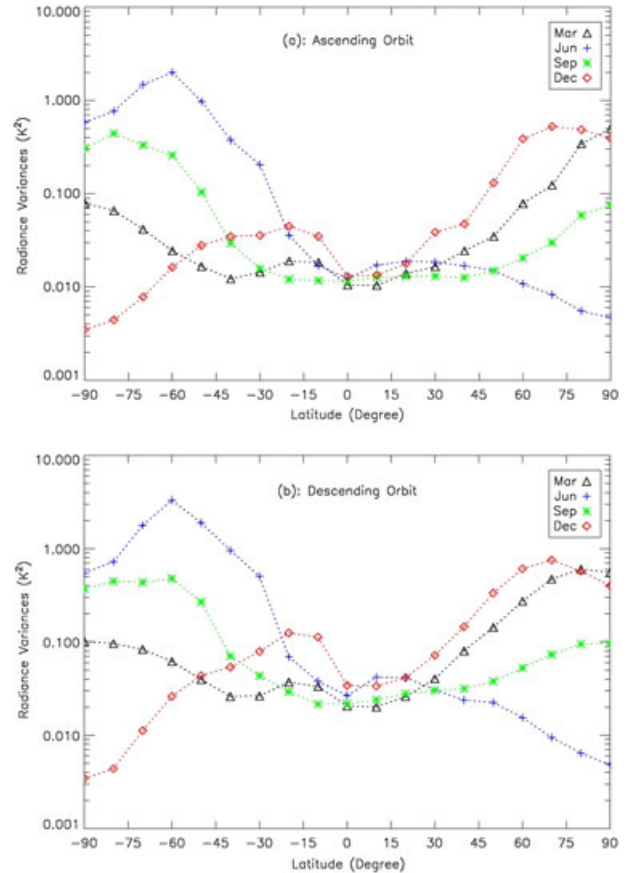


Figure 5. The final variance thresholds that are used in this study to detect gravity wave peak events. March, June, September, and December are shown for (a) ascending and (b) descending orbits separately.

throughout the year are relatively small. However, much larger differences exist at high latitudes. Maximum thresholds appear in winter, while minima are found in summer. Thresholds at the March equinox are larger than those at the September equinox.

3.2. Seasonal Means

[24] By applying the detection method outlined in the previous section, we calculated seasonal peak event frequencies of stratospheric gravity waves based on a 9 year record (2003 to 2011) of AIRS observations. The large amount of data gathered during that time period allows us to estimate the peak event frequencies with high accuracy, even for a horizontal grid with fine sampling. Data are binned into an $0.5^\circ \times 0.5^\circ$ longitude-latitude grid. As a first step, we calculated monthly peak event frequencies for the whole measurement period. Taking into account the AIRS data coverage (section 2.1), it can be concluded that the frequencies have a sampling error (reciprocal number of total counts) better than 0.7%. Next we averaged the monthly means for different seasons, giving each month equal weight to homogenize the results. We carried out the analysis for four different seasons, i.e., for November to February (NDJF), March and April (MA), May to August (MJJA), and September and October (SO). The sampling error for the 9 year seasonal averages is better than 0.02% (NDJF and MJJA) and 0.04% (MA and SO), respectively. As

discussed above, the analysis was carried out separately for daytime and nighttime.

[25] Figures 6 and 7 show the results. The maps reveal numerous hotspots of gravity wave peak events rather than a homogeneous distribution over the globe. Please note that the longitudinal variability in each map is based on a fixed detection threshold. However, differences between daytime and nighttime, from latitude to latitude, or from season to season are not only due to atmospheric variability, but also caused by differences in the detection thresholds. *Hoffmann and Alexander* [2010] gave an example of how different thresholds restrict the gravity wave detection in terms of horizontal and vertical wavelengths. Following linear wave theory and considering a saturation limit, they showed that for a wave with 5 K amplitude at 30 km altitude, a threshold of 0.01 K^2 restricts the detection to vertical wavelengths larger than 13 km and horizontal wavelengths smaller than 1150 km. For a threshold of 0.1 K^2 the wavelength limits are at 17 km (vertically) and 1000 km (horizontally). For 1 K^2 the limits are at 30 km and 800 km. The different thresholds should be taken into account when comparing peak event frequencies for different latitudes, seasons, or time of day.

[26] We present the individual gravity wave hotspots in detail in section 5, but here we discuss a few of the most prominent features. During the season from November to February (NDJF) the largest hotspot of gravity wave peak events is found over Brazil in South America (Figures 6a

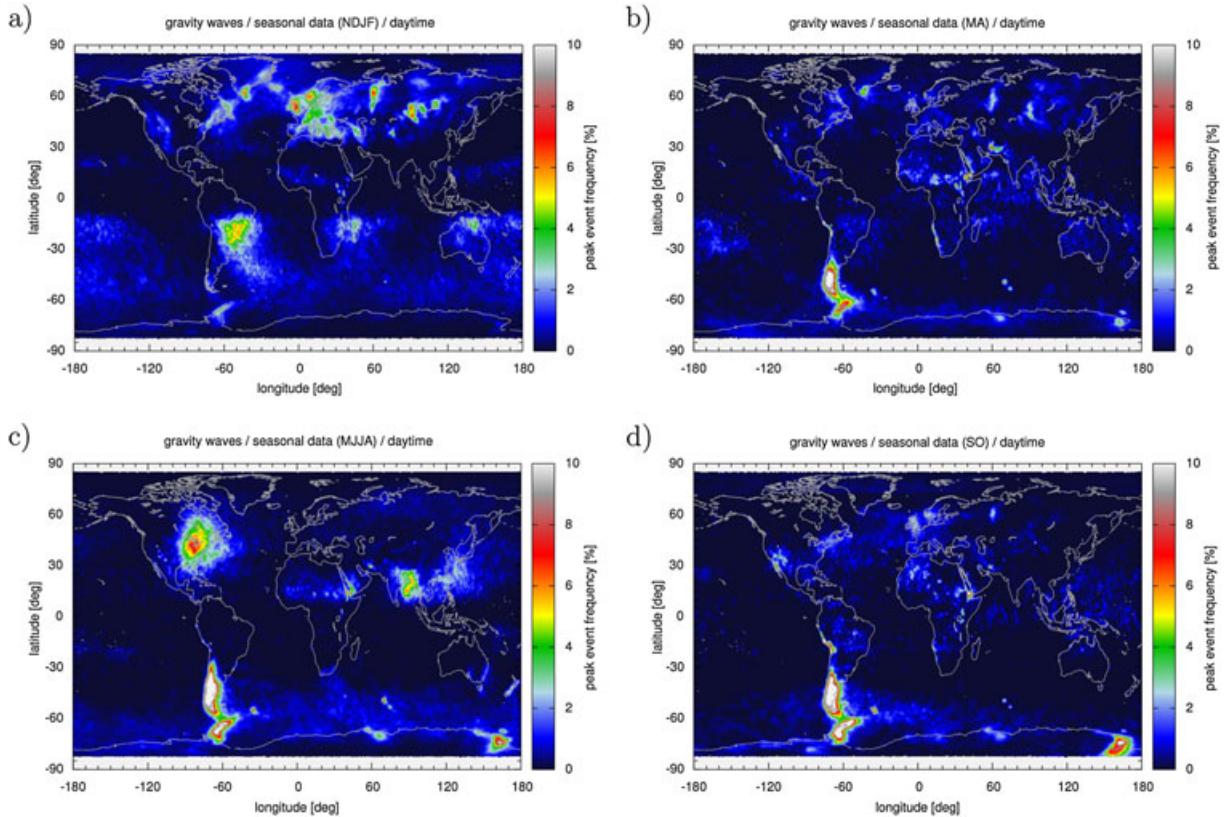


Figure 6. Seasonal peak event frequencies of gravity waves at daytime as obtained from AIRS observations during the years 2003 to 2011. The maps combine data for (a) November to February, (b) March and April, (c) May to August, and (d) September and October.

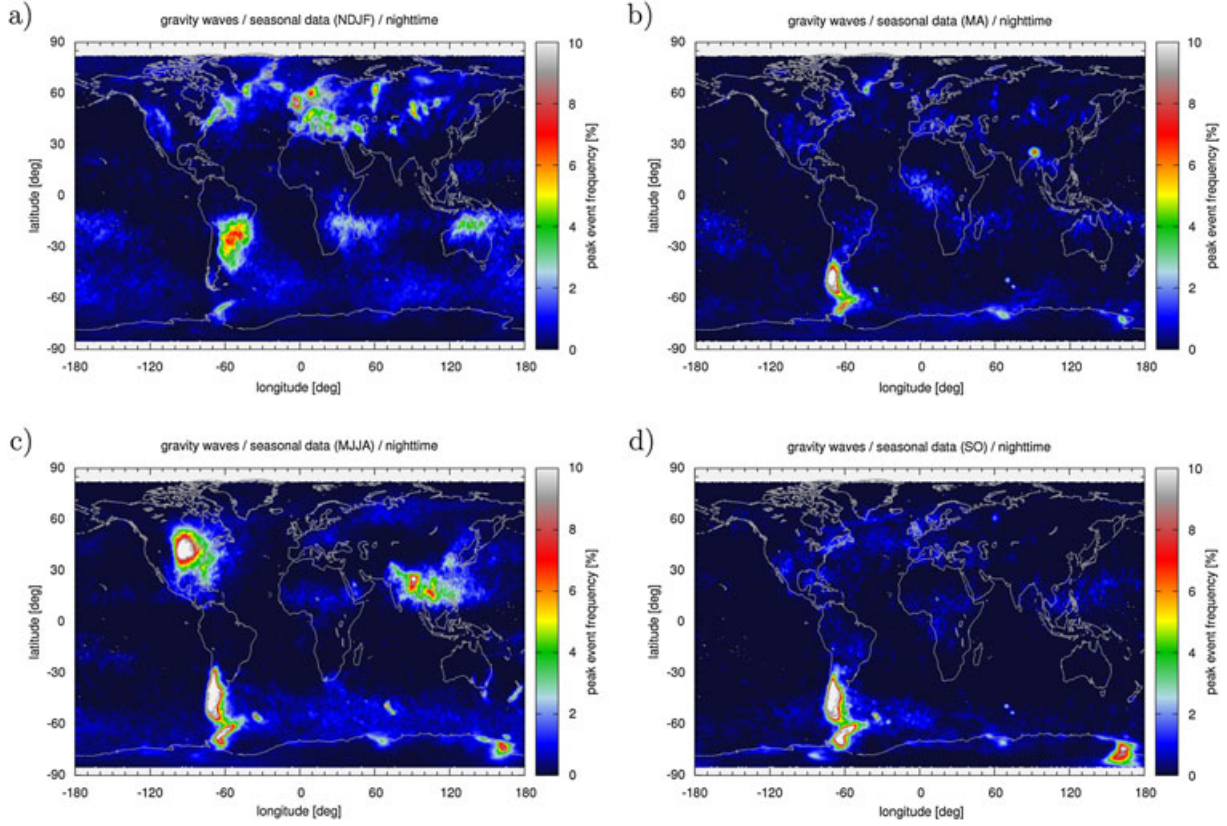


Figure 7. Same as Figure 6, but for nighttime.

and 7a). For the season from May to August (MJJA) large areas with peak events are found near Patagonia and the Antarctic Peninsula, over the North American Great Plains, and south of the Himalayas (Figures 6c and 7c). During March and April (MA) as well as September and October (SO) the hotspots near Patagonia and the Antarctic Peninsula are again most prominent (Figures 6b and 6d and Figures 7b and 7d).

[27] An outstanding feature of the maps presented here is the large number of mesoscale hotspots, mostly found close to prominent orographic features like mountain ranges, coasts, lakes, deserts, or isolated islands. These mesoscale hotspots are made visible by means of the high spatial resolution and the large amount of AIRS observations as well as the careful selection of the detection thresholds. However, it should be taken into account that the method for gravity wave detection used here considers only local measurements. Gravity waves that are generated by sources with fixed geographic locations are more likely found to be related to a hotspot compared with gravity waves that are caused by moving or more randomly located wave sources.

4. Correlations With Convection

4.1. Detection of Convection

[28] The detection of deep convective clouds in AIRS observations is discussed in detail by *Aumann et al.* [2006, 2007, 2008, 2011]. The detection is based on the analysis of radiances in spectral window regions. Low brightness temperatures indicate high cold clouds whereas high brightness

temperatures are sensed for low clouds or surface emissions for clear air. *Aumann et al.* [2006] used a brightness temperature threshold of 210 K at $8.1 \mu\text{m}$ (1231.3 cm^{-1} , AIRS channel number 1291) to detect deep convective clouds at tropical latitudes. *Aumann et al.* [2011] detected high cold clouds, i.e., a mix of deep convective clouds and cold anvil clouds, if the brightness temperature at $8.1 \mu\text{m}$ drops below 225 K. *Aumann et al.* [2006, 2007, 2008] identified about 6000 large thunderstorms in AIRS data each day, almost exclusively within $\pm 30^\circ$ of the equator.

[29] In the study of *Hoffmann and Alexander* [2010] it was found that a threshold of 210 K is too low to detect most of the strong convective events at middle latitudes. A visual inspection of the detection results indicated that a substantial number of large thunderstorms and mesoscale convective systems was missing. This is related to the tropopause temperatures, which are higher at middle latitudes (about 215 to 220 K) than in the tropics (about 195 to 200 K). See Figure 8 for zonal means at different months. Significant overshooting would be required to reach a detection threshold of 210 K at middle latitudes. Hence, the threshold was raised to 220 K in that study.

[30] In this study, we found that detection methods with constant thresholds do not work on a global scale because they tend to cause large numbers of ambiguous detections at different latitudes or seasons. Hence, we introduced latitudinally and monthly varying detection thresholds. These are based on a monthly mean zonal mean tropopause temperature climatology derived from NCAR/NCEP reanalysis (see Figure 8). *Romps and Kuang* [2009] used the same

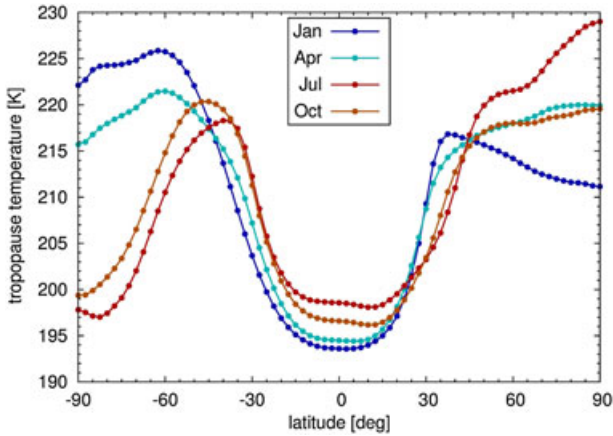


Figure 8. Zonal mean tropopause temperatures from NCAR/NCEP reanalysis for different months.

approach to detect overshooting convection in tropical cyclones.

[31] Another problem that had to be addressed occurs when the surface temperatures are cold, such as at high latitudes or for elevated terrain (like the Plateau of Tibet). In this case a discrimination between cloud-free and cloudy scenes is sometimes not possible because of a lack of substantial difference between the surface temperature and the mean tropopause temperature. To identify this kind of situation, we calculated monthly mean $8.1 \mu\text{m}$ brightness temperatures (see Figure 9 for an example). Based on a comparison with the detection results, we concluded that the method does not work if the monthly mean brightness temperatures drop below 250 K at middle or high latitudes. The criterion is not applied at tropical latitudes (within $\pm 25^\circ$ latitude) because deep convection can be prevalent. Even mean brightness temperatures can drop below 250 K in certain places in the tropics. An example of this situation is found near Eastern Indonesia and Papua New Guinea in Figure 9. However, at tropical latitudes the direct detection of deep convection based on $8.1 \mu\text{m}$ brightness temperatures is always unambiguous.

4.2. Seasonal Means

[32] Figures 10 and 11 show seasonal means of the occurrence frequencies for convection, identified using the

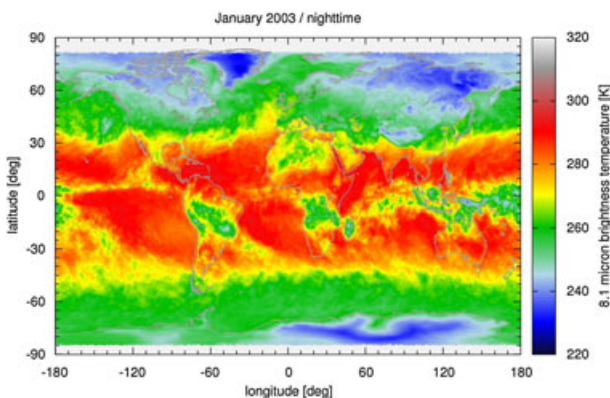


Figure 9. Monthly mean $8.1 \mu\text{m}$ brightness temperatures in January 2003 from AIRS nighttime measurements.

detection method described in the previous section. The statistical analysis is based on the same approach as outlined for the gravity waves in section 3.2. In this case daytime and nighttime data are directly comparable because the same thresholds are applied for detection. However, detection thresholds do vary with latitude and month. In this section, we present briefly the regions and seasons with prominent convective activity.

[33] In NDJF, significant convective activity (exceeding the 0.5% level) is found near Patagonia, the Antarctic Peninsula, southern Brazil, the Atlantic Ocean close to the United States, northern Australia, the Coral Sea, and the Bering Sea (Figures 10a and 11a). Convective activity is also observed in smaller areas, e.g., near the Canadian Rocky Mountains, Iceland, and central Africa. In MJJA strong activity is found near Patagonia, South Brazil, Central America, the North American Great Plains, central Africa, and Southeast Asia (Figures 10c and 11c). The intermediate seasons MA and SO show similar patterns of convective activity, but additional areas with increased activity are found, e.g., over the South Atlantic (Figure 11d) and central Asia (Figure 11b).

[34] Our analysis shows prevalent activity due to deep convection in the tropics and due to mesoscale convective systems and large thunderstorms at middle and high latitudes. Deep convection at the intertropical convergence zone is best visible in MJJA and SO. During all seasons the observed occurrence frequencies are only slightly larger during the nighttime. *Sassen et al.* [2009] pointed out that according to the model usually applied for the diurnal cycle of tropical thunderstorms, the deep convection maxima occur about 6 h prior to both the Aqua day or night overpasses. The absolute values of the occurrence frequencies presented here also need to be considered carefully. A parameter study showed that the absolute values critically depend on the detection thresholds. However, the spatial patterns remain similar if the thresholds are varied.

4.3. Temporal Correlations

[35] A direct comparison of the peak event frequencies for gravity waves (Figures 6 and 7) with the occurrence frequencies for convection (Figures 10 and 11) gives the first indication which gravity wave hotspots are potentially related to convective sources. However, such a comparison does not take into account the large intraseasonal variability of the processes we are looking at. Hence, we also analyzed temporal correlations of time series of gravity wave and convective events to improve the source classification. For this purpose, we calculated daily means from the AIRS detections of gravity waves and convection on a horizontal grid with $5^\circ \times 5^\circ$ sampling. A coarser grid was chosen here to improve the sampling error (about 0.2% for the daily means). Furthermore, a coarse grid accounts better for horizontal propagation of the gravity waves, i.e., for displacements between the location of a tropospheric source and a stratospheric detection.

[36] As an example, Figure 12 presents time series for two regions with significant gravity wave peak event frequencies. The first region (Figure 12a) is located over the North American Great Plains and shows gravity waves that are mainly due to convection during the summer thunderstorm season [Hoffmann and Alexander, 2010]. The second region

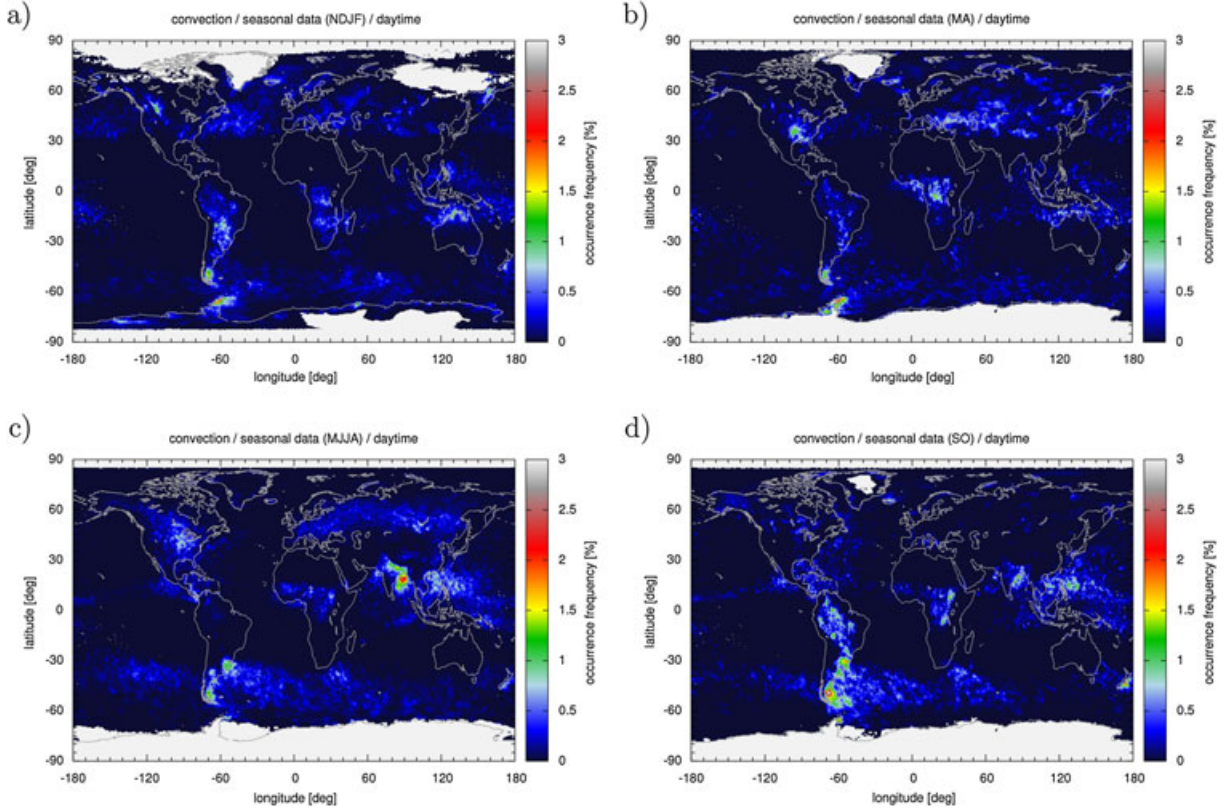


Figure 10. Seasonal occurrence frequencies of convection at daytime as obtained from AIRS observations during the years 2003 to 2011. The maps combine data for (a) November to February, (b) March and April, (c) May to August, and (d) September and October. White patches indicate areas where detection is not possible because of low surface temperatures.

(Figure 12b) is located near Patagonia and shows gravity waves that are mainly triggered by orographic generation at the Andes mountains. Looking at the occurrence frequencies for convection only, one might conclude that convection is a significant source mechanism for both regions. However, the correlation analysis shows that the time series for the North American Great Plains are statistically associated whereas the data for the Andes region are not.

[37] To quantitatively infer the degree of temporal correlation, we calculated the Spearman rank-order correlation coefficients [e.g., *Press et al.*, 2002] of the time series. Compared with the standard Pearson correlation coefficient, the rank-order correlation coefficient is sensitive not only to linear correlation, but to almost any kind of statistical association and it is more robust against outliers. For the correlation analysis, we combine the time series data for daytime and nighttime and for all seasons. Although the individual occurrence frequencies are based on variable detection thresholds, the Spearman correlation coefficient is not significantly affected because it depends only on the rank-order and not on the absolute values of the time series data.

[38] Figure 13 presents the results of the correlation analysis. The correlation coefficients are in the range from zero (no correlation) to 0.5 (a medium degree of statistical association). As expected, anticorrelations between gravity waves and convection are not found. Correlations are observed for gravity wave hotspots over the North American

Great Plains, South Brazil, and Southeast Asia. Correlations are generally low in the tropics because of the wind filtering and visibility effects described in section 3.1, which makes it difficult to observe gravity waves in AIRS data in the tropics. Please note that low correlations are found for well-known mountain wave hotspots, e.g., the Andes or the Scandinavian mountain ranges. The correlation analysis provides an important piece of information for the classification of the source mechanisms of the gravity wave hotspots.

5. Convective and Orographic Hotspots

5.1. Identification and Classification

[39] This section of the paper presents the gravity wave hotspots located with the AIRS observations and the detection methods presented in sections 3 and 4. Results for different seasons are shown on global maps in Figures 14 and 15 for daytime and nighttime, respectively. Red dots indicate the locations of the hotspots. The gray contour surface shows the zonal terrain slope, based on the global relief model data of *Amante and Eakins* [2009]. In addition, Tables 1 to 8 list the center location and surface area of each hotspot, the maximum peak event frequency for gravity waves ($f_{\text{GW,max}}$), the maximum occurrence frequency for convection ($f_{\text{DC,max}}$), the rank-order correlation coefficient between the gravity wave and convection time series (ρ_{DC}), and the maximum zonal terrain slope (dz_{max}). In order

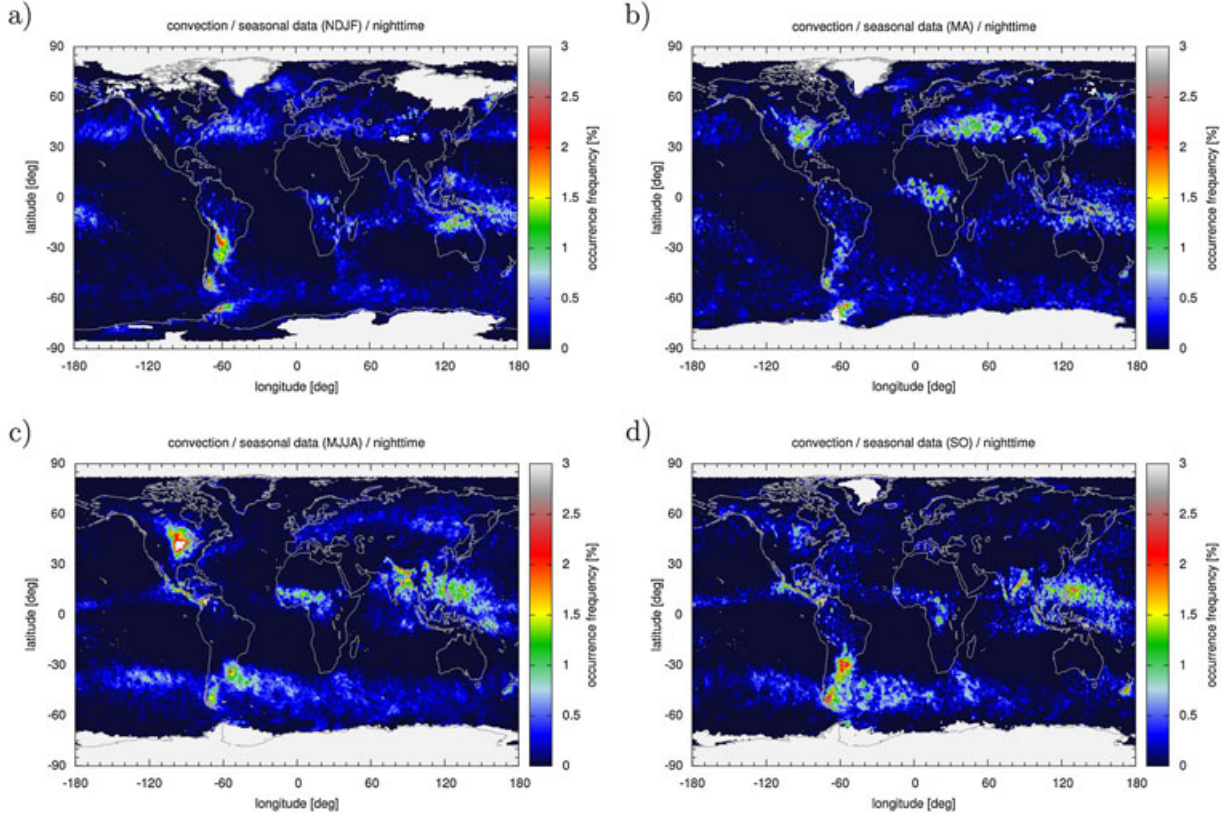


Figure 11. Same as Figure 10, but for nighttime.

to limit the presentation to statistically significant results, ρ_{DC} is only reported if $f_{DC,max}$ exceeds a minimum value of 0.01%.

[40] We define a particular region on the globe to be a gravity wave hotspot if the peak event frequency exceeds a threshold of 5%. This value is an ad hoc choice, based on visual inspection of the results. Parameter studies show that minor variations of the threshold (i.e., values from 4 to 6%) lead to similar spatial and temporal distributions of hotspots. A simple clustering method is applied to find the neighboring grid points for each hotspot. A running index is assigned to each hotspot, which we refer to in the text below and which allows the reader to identify the hotspots in Figures 14 and 15 and Tables 1 to 8. Within each table the hotspots are sorted according to their surface area.

[41] A classification of hotspots in terms of source mechanisms is also presented in Tables 1 to 8. We classify a hotspot as convective (label “c”) if $f_{DC,max}$ exceeds a threshold of 0.2% and ρ_{DC} exceeds a threshold of 0.1. If it is not classified as convective, we classify a hotspot as orographic (label “o”) if dz_{max} exceeds a threshold of 20 m/km. Otherwise, the hotspot remains unclassified. The thresholds for classification were tuned to provide reasonable results for well-known hotspots. However, because we selected rather simple criteria for classification, the results presented here offer only a first guideline and may be overruled by expert judgment and more detailed studies at a later stage. Table 9 presents a global summary of the hotspot detection and classification.

5.2. North America

[42] The largest hotspot (index 60) of gravity wave peak event frequencies in North America is found over the Great Plains during boreal summer nighttime. A maximum peak event frequency of 16% is observed. There is a clear overlap with a pattern of convection (4.8% maximum occurrence frequency). A rank-order correlation coefficient of 0.38 also indicates that convection is the major source for gravity waves in this region. The hotspot is present in the daytime as well (index 49). The mean occurrence frequencies of convective waves during the North American thunderstorm season were studied in detail based on AIRS measurements by Hoffmann and Alexander [2010]. Mesospheric wave observations by an OH airglow imager in this region (near Fort Collins, Colorado) were presented by Yue *et al.* [2009] and related to multiple convective storms by Vadas *et al.* [2012].

[43] In boreal summer nighttime, we find another hotspot (index 68) of gravity wave peak event frequencies about 300 km southeast of the coast of Carolina over the Atlantic Ocean. For this hotspot a rank-order correlation of 0.12 is observed. Hurricanes are an important source of gravity waves in this region [e.g., Kuester *et al.*, 2008].

[44] In boreal spring and autumn daytime, a strong hotspot (index 29 and 77) of gravity wave peak event frequencies (up to 17%) is found over the Baja California Peninsula and the Gulf of California. Low occurrence frequencies for convection and a rank-order correlation coefficient near zero indicate that convection is not relevant as a source for this

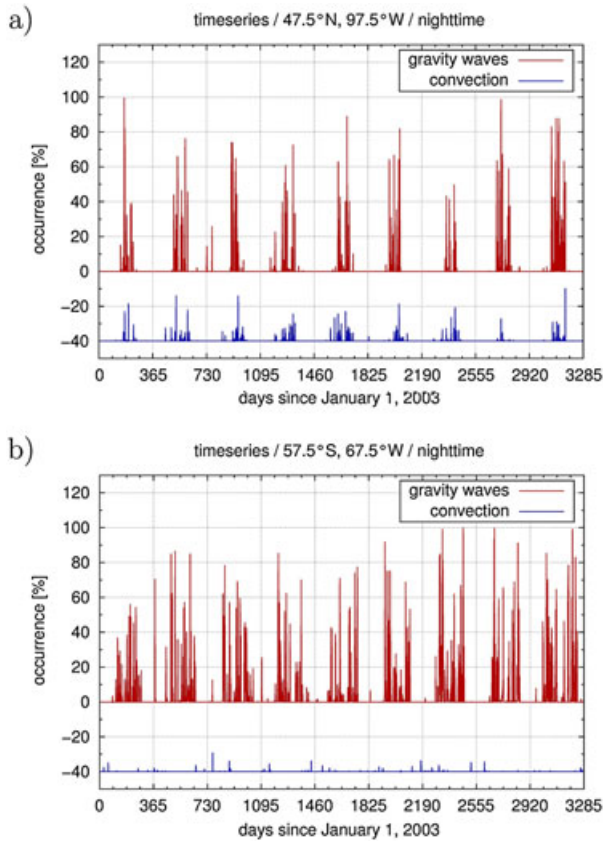


Figure 12. Daily time series of occurrence frequencies for gravity waves (red) and convective events (blue) from AIRS observations during the years 2003 to 2011. Data are shown for $5^\circ \times 5^\circ$ grid boxes in (a) North America and (b) South America (see plot titles for center location). Time series for convection are shown with an offset of -40% .

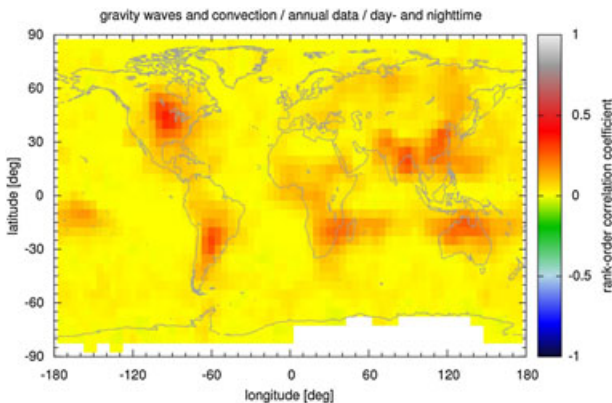


Figure 13. Map of rank-order correlation coefficients between local time series of gravity waves and convective events (compare Figure 12 for examples).

hotspot. Frey *et al.* [2000] presented OH airglow imager measurements for this region (from Mt. Laguna observatory, California, in March 1998), but did not relate the observed waves to a source mechanism. In autumn daytime, a minor orographic hotspot (index 86) is found in Arizona. Brintjes *et al.* [1994] presented a modeling case study for this area.

[45] The boreal winter season is mostly quiet, but the southern tip of Greenland is a persistent hotspot (index 6 and 43) of gravity wave peak event frequencies at daytime and nighttime. Doyle and Shapiro [1999] and Limpasuvan *et al.* [2007] discussed the flow response to large-scale topography for the Greenland tip jet and its implications for gravity wave generation. Minor hotspots (index 21 and 23) at nighttime are found near Newfoundland and the northern Appalachians.

[46] In this study, the Rocky Mountains do not show up prominently in the boreal winter season. Maximum peak event frequencies are about 2% (Figures 6a and 7a). A long-term climatology (1981–2010) of NCAR/NCEP reanalysis shows that the zonal winds at 10 hPa are about 0 to 20 m/s for the area of the Rocky Mountains. However, the zonal wind in this region is not strong enough to allow gravity waves with long vertical wavelengths to propagate into the stratosphere; and the AIRS observations are limited to those long vertical wavelengths. In contrast, zonal winds up to 30 to 50 m/s are observed for an area extending from 60°W to 120°E and 40°N to 70°N . This area includes nearly all the hotspots found at northern middle and high latitudes in boreal winter.

5.3. South America

[47] The largest hotspot of gravity wave peak event frequencies in South America is found over the southern Andes. This hotspot persists from austral autumn to spring during daytime and nighttime (index 26, 44, 48, 61, 71, 87). Maximum peak event frequencies vary from 20 to 31%. Occurrence frequencies for convection are large (up to 3.6%), but the rank-order correlation coefficients indicate only weak correlation with gravity wave peak event frequencies. This indicates that the observed waves are mainly mountain waves. This hotspot is one of the largest and strongest globally and was readily identified from early satellite-based studies on small-scale temperature fluctuations in the stratosphere [Eckermann and Preusse, 1999; McLandress *et al.*, 2000; Jiang *et al.*, 2002]. Global estimates of gravity wave momentum flux show that this region is an important source for waves contributing to Southern Hemisphere wind drag [Ern *et al.*, 2004; Alexander *et al.*, 2008; Hertzog *et al.*, 2008; Ern *et al.*, 2011].

[48] From austral autumn to spring, up to three gravity wave hotspots are found over the central and northern Andes and the Pacific coast. These hotspots are observed only during daytime. Convective activity is not observed. The hotspot near Piura, Peru persists from March through October (index 38, 57, 79) with peak event frequencies up to 10%. The hotspot near the Cordillera Occidental Mountains (Peru and northern Chile) and the Atacama desert is only observed in the equinox seasons. In autumn we identify two separate hotspots (index 31 and 35) with maximum peak event frequencies of 21% and 17%, respectively. In austral spring we identify this region as one large hotspot (index 74) with a maximum peak event frequency of 32%. This is the global maximum found in this study. Studies of gravity waves in the Andes Cordillera region based on GPS radio occultation data are presented by de la Torre *et al.* [2006] and Llamedo *et al.* [2009].

[49] Finally, in austral summer a large hotspot (index 1 and 11) is observed near South Brazil, Paraguay, and northeast

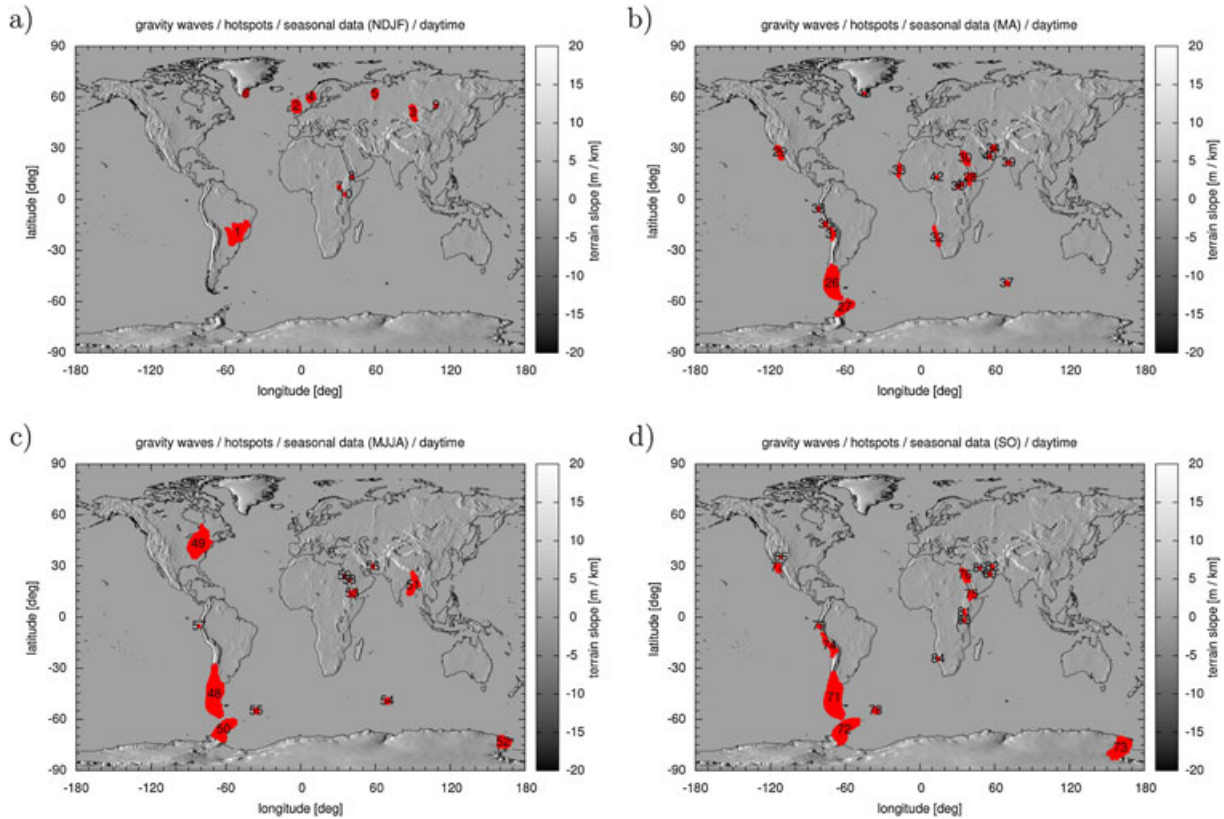


Figure 14. Seasonal hotspots of gravity wave peak event frequencies at daytime. Red dots indicate regions where peak event frequencies of gravity waves exceed the 5% level. The gray contour surface illustrates the zonal terrain slope.

Argentina. We find maximum peak event frequencies for gravity waves of 6.8 and 8.3% at daytime and nighttime, respectively. An occurrence frequency for convection of 2.4% and a rank-order correlation coefficient of 0.28 at nighttime show that convection is the major source mechanism. Based on OH airglow observations near Brasilia, Brazil, *Vadas et al.* [2009] showed that convection is likely the source of mesospheric gravity waves in this region.

5.4. Europe

[50] Gravity wave hotspots over Europe are observed only during the boreal winter season. Maximum peak event frequencies are typically in the range from 5 to 10%. Persistent hotspots are found over the United Kingdom (index 2 and 12), southern Norway and Sweden (index 4 and 13), and the Urals (index 5 and 16). During nighttime we found four more hotspots near the Massif Central, France (index 19), the Jura and Vosges mountains, France, the Swiss Alps, and the Black Forest, Germany (index 15), the western Carpathian Mountains and Transylvanian Alps, Romania (index 24), and the Pindus mountains, Greece (index 17). These are all orographic features, i.e., correlations with convection were not found. The nighttime features are also present in the daytime, but the maximum peak event frequencies are around 4% and they are not identified as hotspots. The day and night difference cannot be explained by differences in the detection thresholds. The northern midlatitude NDFJ nighttime thresholds exceed the daytime

thresholds by a factor ~ 2 , i.e., we would expect a larger number of detections at daytime.

[51] Mountain waves at high latitudes, in particular near Scandinavia, have been studied because of their relevance for the formation of polar stratospheric clouds and Arctic ozone loss [*Carlaw et al.*, 1998; *Dörnbrack et al.*, 1999, 2002]. Even the early satellite-based study of *Eckermann and Preusse* [1999] identified the extended mountain ranges in and around central Eurasia as a major source of stratospheric mountain wave activity. In a dedicated study, *Jiang et al.* [2004] analyzed data from the Microwave Limb Sounder aboard the UARS during the Northern Hemisphere winters from 1994 to 1997. The hotspots over Europe, North America, and Asia identified from the UARS Microwave Limb Sounder radiance variances agree well with those found in this study. Recent studies based on GPS radio occultation data have also isolated mountain wave climatological enhancements over Greenland, Scandinavia, and central Asia [*Alexander et al.*, 2009b]. However, it should be noted that our study provides results at higher horizontal resolution and covers a longer time period than earlier studies based on satellite limb and occultation data.

5.5. Asia

[52] The largest hotspots in Asia were found from March to August over the Bay of Bengal and north to the Himalayas (index 46, 51, 62) and over the Indochina Peninsula (index 63). Peak event frequencies become as

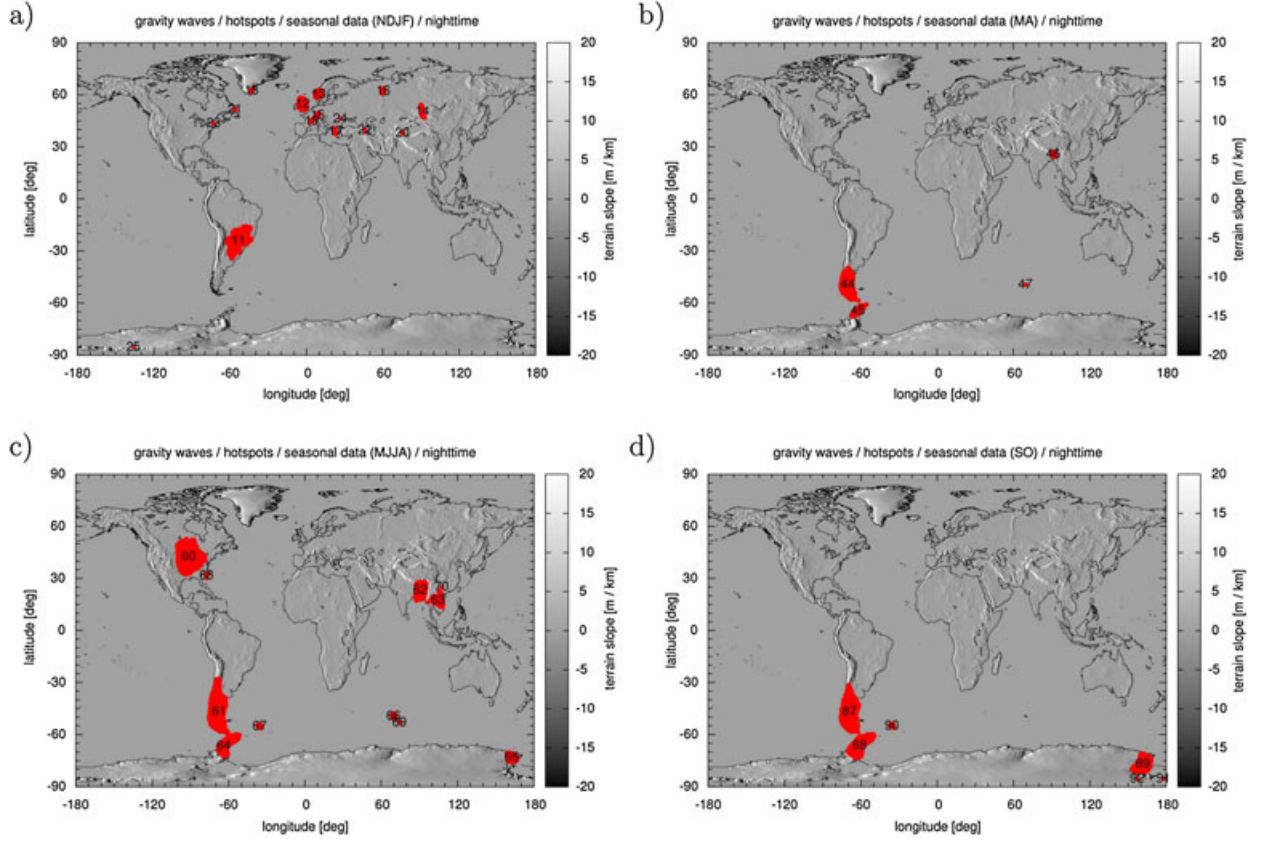


Figure 15. Same as Figure 14, but for nighttime.

Table 1. Seasonal Hotspots (NDJF) of Gravity Wave Peak Event Frequencies at Daytime

Index	Location	Area [km ²]	$f_{\text{GW,max}}[\%]$	$f_{\text{DC,max}}[\%]$	ρ_{DC}	$\text{dz}_{\text{max}}[\text{m/km}]$	Class
1	(19.5°S, 50.2°W)	691,300	6.83	0.94	0.16	31	c
2	(54.7°N, 2.8°W)	205,200	7.83	0.61	0.06	27	o
3	(50.9°N, 90.8°E)	169,200	7.20	0.98	0.03	83	o
4	(60.0°N, 9.0°E)	103,300	6.63	0.39	0.02	79	o
5	(62.1°N, 60.1°E)	80,900	7.41	0.64	0.04	58	o
6	(62.2°N, 43.4°W)	40,300	6.62	0.61	0.02	68	o
7	(7.2°N, 31.5°E)	12,200	9.21	0.00	-	2	-
8	(13.6°N, 42.1°E)	9,000	9.78	0.00	-	30	o
9	(55.1°N, 109.2°E)	7,100	5.45	0.14	0.07	59	o
10	(3.0°N, 36.2°E)	6,200	5.62	0.00	-	4	-

Table 2. Seasonal Hotspots (NDJF) of Gravity Wave Peak Event Frequencies at Nighttime

Index	Location	Area [km ²]	$f_{\text{GW,max}}[\%]$	$f_{\text{DC,max}}[\%]$	ρ_{DC}	$\text{dz}_{\text{max}}[\text{m/km}]$	Class
11	(24.1°S, 53.5°W)	1,888,300	8.32	2.44	0.28	38	c
12	(54.7°N, 3.2°W)	281,300	10.04	0.43	0.06	27	o
13	(60.4°N, 9.4°E)	127,900	7.27	0.49	0.02	79	o
14	(50.4°N, 90.9°E)	108,000	6.91	1.23	0.03	83	o
15	(48.2°N, 8.6°E)	45,300	6.02	0.32	0.03	105	o
16	(62.2°N, 60.1°E)	44,600	6.43	1.33	0.04	23	o
17	(38.9°N, 22.6°E)	33,600	5.52	0.18	0.05	66	o
18	(62.4°N, 43.3°W)	20,000	5.43	1.48	0.02	68	o
19	(44.9°N, 3.8°E)	19,700	5.41	0.20	0.02	37	o
20	(38.0°N, 75.5°E)	9,700	5.60	0.00	-	55	o
21	(51.5°N, 56.0°W)	7,700	5.31	0.17	0.00	10	-
22	(39.6°N, 46.1°E)	7,100	5.10	0.10	0.01	64	o
23	(43.6°N, 72.9°W)	6,700	5.34	0.06	0.10	25	o
24	(46.2°N, 26.8°E)	2,100	5.21	0.44	0.07	21	o
25	(85.2°S, 135.8°W)	300	7.92	0.00	-	13	-

Table 3. Seasonal Hotspots (MA) of Gravity Wave Peak Event Frequencies at Daytime

Index	Location	Area [km ²]	$f_{\text{GW,max}}[\%]$	$f_{\text{DC,max}}[\%]$	ρ_{DC}	$\text{dz}_{\text{max}}[\text{m/km}]$	Class
26	(49.2°S, 70.0°W)	1,202,100	22.06	1.80	0.05	148	o
27	(63.3°S, 59.9°W)	269,900	8.75	3.62	0.07	112	o
28	(12.8°N, 40.7°E)	135,400	25.06	0.03	0.14	67	o
29	(27.5°N, 112.3°W)	131,300	17.40	0.00	-	44	o
30	(24.2°N, 36.6°E)	106,900	13.83	0.00	-	33	o
31	(20.4°S, 69.9°W)	75,200	20.63	0.00	-	67	o
32	(22.6°S, 14.0°E)	71,100	22.91	0.00	-	31	o
33	(17.0°N, 16.3°W)	61,900	12.59	0.00	-	1	-
34	(30.0°N, 59.1°E)	48,100	11.50	0.03	0.02	84	o
35	(14.5°S, 75.5°W)	41,800	17.37	0.00	-	67	o
36	(7.6°N, 30.9°E)	24,500	8.92	1.11	0.06	0	-
37	(49.2°S, 69.9°E)	18,100	6.21	0.37	0.00	34	o
38	(5.7°S, 81.0°W)	15,400	9.61	0.00	-	4	-
39	(21.6°N, 71.5°E)	14,400	10.33	0.00	-	4	-
40	(25.2°N, 56.2°E)	14,000	12.73	0.00	-	23	o
41	(9.0°N, 34.2°E)	6,100	6.47	0.03	0.06	23	o
42	(13.0°N, 13.8°E)	6,000	6.64	0.00	-	0	-
43	(62.2°N, 44.2°W)	1,400	5.16	0.00	-	10	-

Table 4. Seasonal Hotspots (MA) of Gravity Wave Peak Event Frequencies at Nighttime

Index	Location	Area [km ²]	$f_{\text{GW,max}}[\%]$	$f_{\text{DC,max}}[\%]$	ρ_{DC}	$\text{dz}_{\text{max}}[\text{m/km}]$	Class
44	(49.3°S, 69.9°W)	1,176,800	19.52	1.92	0.10	148	o
45	(64.3°S, 62.1°W)	165,600	8.71	2.94	0.11	112	c
46	(25.8°N, 91.4°E)	105,600	9.10	0.95	0.26	79	c
47	(49.2°S, 69.5°E)	4,000	5.36	0.28	0.00	34	o

Table 5. Seasonal Hotspots (MJJA) of Gravity Wave Peak Event Frequencies at Daytime

Index	Location	Area [km ²]	$f_{\text{GW,max}}[\%]$	$f_{\text{DC,max}}[\%]$	ρ_{DC}	$\text{dz}_{\text{max}}[\text{m/km}]$	Class
48	(45.2°S, 69.0°W)	1,997,300	27.79	1.94	0.10	148	o
49	(43.0°N, 81.9°W)	1,243,400	8.27	1.00	0.22	30	c
50	(65.9°S, 61.6°W)	490,400	17.31	2.66	0.07	122	o
51	(18.6°N, 90.3°E)	324,100	6.60	2.49	0.29	43	c
52	(73.4°S, 162.7°E)	144,100	9.92	0.00	-	236	o
53	(13.9°N, 41.4°E)	65,900	10.68	0.61	0.14	67	c
54	(49.1°S, 69.7°E)	40,400	11.14	0.29	0.00	34	o
55	(55.0°S, 35.5°W)	30,100	7.75	0.35	0.00	67	o
56	(29.8°N, 58.0°E)	10,700	7.73	0.00	-	84	o
57	(5.2°S, 81.2°W)	3,100	5.52	0.00	-	1	-
58	(21.8°N, 39.2°E)	2,900	5.33	0.00	-	3	-
59	(24.2°N, 35.2°E)	2,800	6.09	0.00	-	23	o

Table 6. Seasonal Hotspots (MJJA) of Gravity Wave Peak Event Frequencies at Nighttime

Index	Location	Area [km ²]	$f_{\text{GW,max}}[\%]$	$f_{\text{DC,max}}[\%]$	ρ_{DC}	$\text{dz}_{\text{max}}[\text{m/km}]$	Class
60	(42.6°N, 91.0°W)	2,759,800	15.98	4.84	0.38	30	c
61	(46.7°S, 67.2°W)	2,547,900	31.21	2.11	0.10	148	o
62	(23.2°N, 90.8°E)	790,600	11.91	3.44	0.26	112	c
63	(17.5°N, 104.8°E)	444,200	9.39	2.50	0.20	57	c
64	(66.3°S, 63.5°W)	339,500	15.39	1.13	0.07	112	o
65	(73.1°S, 162.5°E)	134,200	8.63	0.00	-	236	o
66	(49.2°S, 69.8°E)	74,500	16.91	0.46	0.00	34	o
67	(55.1°S, 35.4°W)	49,500	9.82	0.43	0.00	67	o
68	(31.8°N, 77.1°W)	18,400	5.58	0.38	0.12	0	c
69	(53.0°S, 74.5°E)	7,400	5.48	0.36	0.02	0	-
70	(25.2°N, 107.8°E)	2,800	5.00	1.33	0.22	10	c

Table 7. Seasonal Hotspots (SO) of Gravity Wave Peak Event Frequencies at Daytime

Index	Location	Area [km ²]	$f_{\text{GW,max}}[\%]$	$f_{\text{DC,max}}[\%]$	ρ_{DC}	$\text{dz}_{\text{max}}[\text{m/km}]$	Class
71	(47.3°S, 68.8°W)	1,962,100	28.87	3.55	0.10	148	o
72	(66.2°S, 60.4°W)	649,800	24.32	2.54	0.07	122	o
73	(76.7°S, 161.0°E)	307,200	12.30	0.00	-	338	o
74	(16.9°S, 72.2°W)	277,300	32.36	0.00	-	104	o
75	(13.2°N, 41.4°E)	141,200	25.05	0.91	0.14	67	c
76	(24.8°N, 36.2°E)	126,000	17.04	0.00	-	38	o
77	(29.1°N, 114.0°W)	75,500	10.46	0.06	0.00	44	o
78	(54.8°S, 35.5°W)	51,600	10.72	0.26	0.00	67	o
79	(5.2°S, 80.6°W)	21,500	8.85	0.00	-	47	o
80	(25.2°N, 56.2°E)	14,000	14.90	0.00	-	23	o
81	(2.9°N, 35.9°E)	9,200	5.72	0.00	-	53	o
82	(29.6°N, 58.1°E)	8,100	8.77	0.00	-	66	o
83	(2.0°S, 35.8°E)	6,200	6.19	0.00	-	27	o
84	(24.5°S, 14.8°E)	5,600	6.28	0.00	-	13	-
85	(28.8°N, 48.2°E)	2,700	5.16	0.00	-	3	-
86	(35.2°N, 111.2°W)	2,500	5.84	0.00	-	31	o

Table 8. Seasonal Hotspots (SO) of Gravity Wave Peak Event Frequencies at Nighttime

Index	Location	Area [km ²]	$f_{\text{GW,max}}[\%]$	$f_{\text{DC,max}}[\%]$	ρ_{DC}	$\text{dz}_{\text{max}}[\text{m/km}]$	Class
87	(46.7°S, 68.7°W)	2,109,600	31.11	2.98	0.10	148	o
88	(66.1°S, 60.7°W)	704,900	22.12	1.80	0.07	122	o
89	(76.8°S, 161.6°E)	305,900	10.89	0.00	-	294	o
90	(54.8°S, 35.5°W)	56,900	13.22	0.55	0.00	67	o
91	(85.2°S, 177.8°E)	300	5.00	0.00	-	143	o
92	(85.2°S, 157.2°E)	300	5.00	0.00	-	6	-

Table 9. Global Statistics of Gravity Wave Hotspots. The Table Provides the Total Surface Area (A_{tot}) and the Fraction of the Orographic (A_{o}), Convective (A_{c}), or not Classified (A_{nc}) Hotspots

Season	$A_{\text{tot}}[\text{km}^2]$	$A_{\text{o}}/A_{\text{tot}}[\%]$	$A_{\text{c}}/A_{\text{tot}}[\%]$	$A_{\text{nc}}/A_{\text{tot}}[\%]$
NDJF, day	1,324,700	46.4	52.2	1.4
NDJF, night	2,602,300	27.1	72.6	0.3
MA, day	2,243,600	94.5	0.0	5.5
MA, night	1,452,000	81.3	18.7	0.0
MJJA, day	4,355,200	62.4	37.5	0.1
MJJA, night	7,168,800	43.9	56.0	0.1
SO, day	3,660,500	95.9	3.9	0.2
SO, night	3,177,900	100.0	0.0	0.0

large as 12%. Occurrence frequencies for deep convection up to 3.4% and rank-order correlation coefficients up to 0.26 indicate that convection is the major source mechanism for both regions. Deep convection in tropical regions is known to cause strong gravity wave activity in the stratosphere and is responsible for important localized forcings in the mesosphere [McLandress *et al.*, 2000].

[53] In boreal winter, orographic hotspots of gravity waves are observed at the Abakanski Khrebet Mountains, Russia (index 3 and 14), the northern Lake Baikal, Russia (index 9), mountain ranges in South Armenia (index 22), and the Pamir Mountains (index 20). Studies of Avdiushin *et al.* [1994] and Kazimirovsky and Danilov [1997] related observed variations in total ozone content to strong vertical winds and internal gravity waves generated by interaction of horizontal airflow with high mountain ridges. They present observations at the Pamir Mountains as an example.

The Himalayas, in particular the mountain range separating the South Asian subcontinent from the Tibetan Plateau, are not identified as a hotspot of gravity wave peak event frequencies. Like in the case of the Rocky Mountains (section 5.2), low zonal wind (−10 to −20 m/s according to the NCAR/NCEP climatology) does not favor the propagation of gravity waves with long vertical wavelengths.

[54] A daytime hotspot of gravity wave peak event frequencies is found from March to October in a mountain and desert area in eastern Iran (index 34, 56, 82). Peak event frequencies reach values of 12%. Additional hotspots are found over the Musandam Peninsula, Persian Gulf (index 40 and 80), near Kuwait (index 85), and near Gujarat, India (index 39). Based on satellite observations in the Thar Desert, India, Das *et al.* [2011] showed that lower atmospheric heating caused by dust storms can trigger gravity waves in the middle atmosphere.

5.6. Africa

[55] Two strong daytime hotspots of gravity wave peak event frequencies in Africa are found over the Red Sea. The hotspot over the northern Red Sea (index 30 and 76) shows peak event frequencies up to 14% and 17% in boreal spring and autumn, respectively. It splits into two smaller and weaker hotspots (index 58 and 59) in boreal summer. In boreal winter this hotspot is not present. A second hotspot is observed over the southern Red Sea and the Danakil Desert, East Africa (index 8, 28, 53, 75). It is present throughout the year with maximum peak event frequencies up to 25%. For the southern hotspot we find a correlation with convection in boreal summer and autumn, but not in boreal winter and spring. For the northern hotspot correlations with convection are not found. *Magalhaes et al.* [2011] recently pointed out that the Red Sea is an undocumented hotspot of atmospheric gravity waves. However, their study focused on trapped waves in the troposphere.

[56] In March and April daytime, we find two strong hotspots of gravity wave peak event frequencies on the west coast of Africa, in particular near the Namib Desert at 16°S to 27°S (index 32) with 23% peak event frequency and at 13°N to 21°N (index 33) with 13% peak event frequency. The Namib hotspot is also observed in September and October (index 84), but it is much weaker (6% peak event frequency). Minor daytime hotspots in different seasons are found near Lake Chad (index 42), South Sudan (index 7 and 36), Lake Turkana in Kenya and Ethiopia (index 10 and 81), and Lake Natron in Tanzania (index 83). We found no observational or theoretical studies of gravity waves for these regions in the literature.

5.7. Antarctica

[57] The most prominent hotspot (index 27, 45, 50, 64, 72, 88) of gravity wave peak event frequencies in Antarctica is found over the Antarctic Peninsula during austral autumn, winter, and spring. It is an orographic feature related to the polar jet. It is consistently present during both daytime and nighttime. The maximum peak event frequencies increase from 9% in autumn to 24% in austral spring. A second orographic hotspot (index 52, 65, 73, 89) is found at the Transantarctic Mountains in austral winter and spring with peak event frequencies up to 12%.

[58] These well-known orographic features have been analyzed in a large number of observational and modeling studies [*Bacmeister et al.*, 1990; *Wu and Jiang*, 2002; *Jiang et al.*, 2005, 2006; *Wu et al.*, 2006; *Alexander and Teitelbaum*, 2007; *Baumgaertner and McDonald*, 2007; *Vincent et al.*, 2007; *Hertzog et al.*, 2008; *Alexander et al.*, 2009b; *de la Torre et al.*, 2012]. In particular, *Plougonven et al.* [2008] reported occurrence frequency estimates of gravity wave events over the Antarctic Peninsula that compare well with those reported here. Mountain waves generated by the Antarctic Peninsula influence the formation of polar stratospheric clouds and polar ozone loss [*Eckermann et al.*, 2009; *McDonald et al.*, 2009; *Lambert et al.*, 2012].

[59] Finally, islands in the southern oceans can also generate mountain waves [*Wu et al.*, 2006; *Alexander et al.*, 2009a]. We identify South Georgia (index 55, 67, 78, 90) and the Kerguelen Islands (index 37, 47, 54, 66) as strong hotspots

in austral autumn, winter, and spring with maximum peak event frequencies up to 17%. The high horizontal resolution of the AIRS observations allows us to distinguish the Heard Island close to the Kerguelen Islands as a separate hotspot (index 69) in austral winter.

5.8. Australia

[60] No hotspots of gravity wave peak event frequencies were located in Australia. However, the maximum peak event frequencies are close to the 5% threshold both in northern Australia in the austral summer, and near New Zealand in the austral winter. Based on satellite climatologies and field campaigns, both regions are well-known for regular gravity wave activity. In our analysis these regions show up less prominently, which is partly due to the specific stratospheric wind filtering and the limits of the AIRS observations, but is mainly because of the specific way in which hotspots are identified. In particular, the analysis focuses on the detection of strong, intermittent peak events rather than regular, albeit significant gravity wave activity. In no case should it be concluded that certain regions of the globe that do not show up as hotspots in this study are therefore less interesting for gravity wave studies.

6. Conclusions and Outlook

[61] The major accomplishment of this study is a comprehensive overview of hotspots of stratospheric gravity wave peak event frequencies for different seasons during daytime and nighttime. The analysis is based on radiance measurements obtained from the AIRS aboard NASA's Aqua satellite during the years 2003 to 2011. Radiance spectra for nearly 9.6×10^9 satellite footprints are taken into account in the analysis. For each geolocation the analysis is based on local AIRS measurements. Gravity waves generated by stationary sources are therefore preferentially found to be related to hotspots. The hotspots are classified according to source mechanisms for gravity waves, in particular with respect to orographic and convective generation.

[62] For this study, we refined existing detection methods for gravity waves and convection in infrared nadir spectra and made them applicable on a global scale. To detect gravity wave peak events, we introduced 4.3 μm brightness temperature variance thresholds, which depend on latitude, month, and time of day. For the detection of convection, a monthly mean zonal mean tropopause temperature climatology is used. By applying our optimized detection methods, we inferred seasonal statistics of peak event frequencies for gravity waves and occurrence frequencies for convection. A correlation analysis of daily time series of gravity waves and convection provides an additional piece of information for source classification. Terrain slopes are used as a simple proxy to infer if orographic generation could be relevant as a source mechanism.

[63] On a global scale, we find between 4 and 18 hotspots of stratospheric gravity wave peak event frequencies for each season and time of day. The analysis reproduces well-known hotspots of gravity wave activity, e.g., the Andes in Patagonia and the Antarctic Peninsula, which are orographic hotspots, and the North American Great Plains during the summer thunderstorm season, which is a convective feature. However, the most interesting result of this study is the

identification of numerous mesoscale hotspots of gravity wave peak event frequencies, which have been made visible only by means of the high horizontal resolution and long record of the AIRS data. These mesoscale hotspots are mostly found near prominent orographic features like mountain ranges, coasts, lakes, deserts, or isolated islands.

[64] Table 9 presents a global summary of the hotspots. Most of the hotspots are related to orographic features. In terms of total surface area, the orographic hotspots outweigh the convective hotspots by a factor ~ 2 . However, from November to February at daytime and nighttime, and from May to August at daytime, larger fractions of area are covered by convective hotspots. Typically, less than 1–2% of the hotspot area remains unclassified. A single exception is found at March and April daytime, when 5.5% of the area is not classified. At this time the largest unclassified hotspot occurs at the west coast of the Sahara Desert and is likely related to land-sea heating contrasts.

[65] We apply detection thresholds, which are optimized for peak events. Regular gravity wave activity is excluded from detection by means of increased variance thresholds. Concerning the interpretation of the data presented here, it should be noted that specific values of the peak event frequencies are generally smaller than occurrence frequencies, which take all detectable gravity wave events into account. A significant fraction of the gravity waves contributing to momentum flux may also be excluded. The magnitudes of brightness temperature variances at the hotspots may not scale with momentum fluxes. This is most important for regions where the raw brightness temperature variances peak, i.e., for winter middle latitudes and summer subtropical latitudes. Nevertheless, the hotspots we identified indicate potentially important source regions for gravity waves, many of which have not previously been noted.

[66] Furthermore, we would like to note that the analysis presented here is limited by observational constraints of the AIRS instrument. The detection of gravity waves is restricted to long vertical wavelengths (~ 15 km or more), because of the broad vertical weighting functions of the infrared nadir sounding technique. The exact limit for the detectable vertical wavelength depends on the individual brightness temperature variance threshold. Gravity waves with long vertical wavelengths require strong zonal background winds to propagate into the stratosphere. An additional restriction arises from the limited number of overpasses and fixed local times of the satellite observations.

[67] Despite some remaining limitations due to observational constraints of the AIRS instrument, this comprehensive analysis can guide the selection of interesting regions and seasons for future case studies of stratospheric gravity waves. The statistical analyses presented here can be used to validate the gravity wave parameterization schemes in general circulation models, in particular to validate source distributions.

[68] **Acknowledgments.** X. Xue was supported by the Chinese Academy of Sciences (projects KJCX2-EW-J01, KZCX2-EW-QN509), the National Natural Science Foundation of China (41174132, 40804035), and a foundation for the Author of National Excellent Doctoral Dissertation of PR China (201025). M. J. Alexander was supported by The Science of Terra and Aqua NASA contract #NNH11CD34C. AIRS data are distributed by the NASA Goddard Earth Sciences Data Information and Services Center. NCAR/NCEP reanalysis derived data are provided by the NOAA/OAR/ESRL PSD, Boulder, Colorado, USA (from their web site

at <http://www.esrl.noaa.gov/psd/>). We thank Alison Grimsdell, Boulder, Colorado for constructive comments and language corrections.

References

- Alexander, M. J., and C. D. Barnett (2007), Using satellite observations to constrain gravity wave parameterizations for global models, *J. Atmos. Sci.*, **64**(5), 1652–1665.
- Alexander, M. J., and L. Pfister (1995), Gravity wave momentum flux in the lower stratosphere over convection, *Geophys. Res. Lett.*, **22**(15), 2029–2032.
- Alexander, M. J., and H. Teitelbaum (2007), Observation and analysis of a large amplitude mountain wave event over the Antarctic Peninsula, *J. Geophys. Res.*, **112**(D21103), doi:10.1029/2006JD008368.
- Alexander, M. J., and H. Teitelbaum (2011), Three-dimensional properties of Andes mountain waves observed by satellite: A case study, *J. Geophys. Res.*, **116**(D23110), doi:10.1029/2011JD016151.
- Alexander, M. J., et al. (2008), Global estimates of gravity wave momentum flux from High Resolution Dynamics Limb Sounder (HIRDLs) observations, *J. Geophys. Res.*, **113**(D15S18), doi:10.1029/2007JD008807.
- Alexander, M. J., S. D. Eckermann, D. Broutman, and J. Ma (2009a), Momentum flux estimates for South Georgia Island mountain waves in the stratosphere observed via satellite, *Geophys. Res. Lett.*, **36**(12), doi:10.1029/2009GL038587.
- Alexander, S. P., A. R. Klekociuk, and T. Tsuda (2009b), Gravity wave and orographic wave activity observed around the Antarctic and Arctic stratospheric vortices by the COSMIC GPS-RO satellite constellation, *J. Geophys. Res.*, **114**(D17103), doi:10.1029/2009JD011851.
- Amante, C., and B. W. Eakins (2009), ETOPO1 1 arc-minute global relief model: Procedures, data sources and analysis, NOAA Technical Memorandum NESDIS NGDC-24, <http://www.ngdc.noaa.gov/mgg/global/global.html>.
- Aumann, H. H., D. T. Gregorich, S. L. Gaiser, D. F. Hagan, T. S. Pagano, L. L. Strow, and D. Ting (2000), AIRS Level 1B Algorithm Theoretical Basis Document (ATBD) Part 1 (IR), *Tech. rep.*, NASA, http://eosps.gsf.nasa.gov/eos_homepage/for_scientists/atbd.
- Aumann, H. H., et al. (2003), AIRS/AMSU/HSB on the Aqua mission: Design, science objective, data products, and processing systems, in *IEEE Trans. Geosci. Remote Sens.*, vol. **41**, pp. 253–264.
- Aumann, H. H., D. Gregorich, and S. M. DeSouza-Machado (2006), AIRS observations of deep convective clouds, in *SPIE Photonics Conference*, 6301–20, San Diego.
- Aumann, H. H., D. T. Gregorich, S. E. Broberg, and D. A. Elliott (2007), Seasonal correlations of SST, water vapor, and convective activity in tropical oceans: A new hyperspectral data set for climate model testing, *Geophys. Res. Lett.*, **34**(L15813), doi:10.1029/2006GL029191.
- Aumann, H. H., A. Ruzmaikin, and J. Teixeira (2008), Frequency of severe storms and global warming, *Geophys. Res. Lett.*, **35**(L19805), doi:10.1029/2008GL034562.
- Aumann, H. H., S. G. DeSouza-Machado, and A. Behrangi (2011), Deep convective clouds at the tropopause, *Atmos. Chem. Phys.*, **11**(3), 1167–1176.
- Avdiushin, S. I., A. Danilov, and A. A. Starovarov (1994), Variations of the total ozone above the central Asian mountains, *Adv. Space Res.*, **14**(9), 169–176.
- Bacmeister, J. T., M. R. Schoeberl, L. R. Lait, P. A. Newman, and B. Gary (1990), ER-2 mountain wave encounter over Antarctica: Evidence for blocking, *Geophys. Res. Lett.*, **17**(1), 81–84.
- Baumgaertner, A. J. G., and A. J. McDonald (2007), A gravity wave climatology for Antarctica compiled from Challenging Minisatellite Payload/Global Positioning System (CHAMP/GPS) radio occultations, *J. Geophys. Res.*, **112**(D05103), doi:10.1029/2006JD007504.
- Becker, E., and C. McLandress (2009), Consistent scale interaction of gravity waves in the doppler spread parameterization, *J. Atmos. Sci.*, **66**, 1434–1449.
- Bruintjes, R. T., T. L. Clark, and W. D. Hall (1994), Interactions between topographic airflow and cloud/precipitation development during the passage of a winter storm in Arizona, *J. Atmos. Sci.*, **51**(1), 48–67.
- Carlsaw, K. S., et al. (1998), Increased stratospheric ozone depletion due to mountain-induced atmospheric waves, *Nature*, **391**, 675–678.
- Das, S. K., A. Taori, and A. Jayaraman (2011), On the role of dust storms in triggering atmospheric gravity waves observed in the middle atmosphere, *Annales Geophysicae*, **29**(9), 1647–1654.
- de la Torre, A., P. Alexander, P. Llamedo, C. Menéndez, T. Schmidt, and J. Wickert (2006), Gravity waves above the Andes detected from GPS radio occultation temperature profiles: Jet mechanism?, *J. Geophys. Res.*, **33**(L24810), doi:10.1029/2006GL027343.
- de la Torre, A., P. Alexander, R. Hierro, P. Llamedo, A. Rolla, T. Schmidt, and J. Wickert (2012), Large-amplitude gravity waves above the southern

- Andes, the Drake Passage, and the Antarctic Peninsula, *J. Geophys. Res.*, **117**(D02106), doi:10.1029/2011JD016377.
- Dörnbrack, A., M. Leutbecher, R. Kivi, and E. Kyrö (1999), Mountain-wave-induced record low stratospheric temperatures above northern Scandinavia, *Tellus A, Dyn Meteorol Oceanogr*, **51**(5), 951–963.
- Dörnbrack, A., T. Birner, A. Fix, H. Flentje, A. Meister, H. Schmid, E. V. Browell, and M. J. Mahoney (2002), Evidence for inertia gravity waves forming polar stratospheric clouds over Scandinavia, *J. Geophys. Res.*, **D20**, doi:10.1029/2001JD000452.
- Doyle, J. D., and M. A. Shapiro (1999), Flow response to large-scale topography: The Greenland tip jet, *Tellus*, **51**(5), 728–748.
- Durran, D. R., and J. B. Klemp (1987), Another look at downslope winds. Part II: nonlinear amplification beneath wave-overtaking layers, *J. Atmos. Sci.*, **44**(22), 3402–3412.
- Eckermann, S. D., and P. Preusse (1999), Global measurements of stratospheric mountain waves from space, *Science*, **286**(5444), 1534–1537.
- Eckermann, S. D., et al. (2006), Imaging gravity waves in lower stratospheric AMSU-A radiances, part 2: Validation case study, *Atmos. Chem. Phys.*, **6**(11), 3343–3362.
- Eckermann, S. D., J. Ma, D. L. Wu, and D. Broutman (2007), A three-dimensional mountain wave imaged in satellite radiance throughout the stratosphere: Evidence of the effects of directional wind shear, *Quart. J. Roy. Meteorol. Soc.*, **133**, 1959–1975.
- Eckermann, S. D., L. Hoffmann, M. Höpfner, D. L. Wu, and M. J. Alexander (2009), Antarctic NAT PSC belt of June 2003: Observational validation of the mountain wave seeding hypothesis, *Geophys. Res. Lett.*, **36**(L02807), doi:10.1029/2008GL036629.
- Ern, M., P. Preusse, M. J. Alexander, and C. D. Warner (2004), Absolute values of gravity wave momentum flux derived from satellite data, *J. Geophys. Res.*, **109**(D20103), doi:10.1029/2004JD004752.
- Ern, M., P. Preusse, J. C. Gille, C. L. Hepplewhite, M. G. Mlynecak, J. M. Russell III, and M. Riese (2011), Implications for atmospheric dynamics derived from global observations of gravity wave momentum flux in stratosphere and mesosphere, *J. Geophys. Res.*, **116**(D19107), doi:10.1029/2011JD015821.
- Frey, H. U., S. B. Mende, J. F. Arens, P. R. McCullough, and G. R. Swenson (2000), Atmospheric gravity wave signatures in the infrared hydroxyl OH airglow, *Geophys. Res. Lett.*, **27**(1), 41–44.
- Fritts, D. C., and M. J. Alexander (2003), Gravity wave dynamics and effects in the middle atmosphere, *Rev. Geophys.*, **41**(1), doi:10.1029/2001RG000106.
- Gong, J., D. L. Wu, and S. D. Eckermann (2012), Gravity wave variances and propagation derived from AIRS radiances, *Atmos. Chem. Phys.*, **12**(4), 1701–1720.
- Grimsdell, A. W., M. J. Alexander, P. T. May, and L. Hoffmann (2010), Model study of waves generated by convection with direct validation via satellite, *J. Atmos. Sci.*, **67**(5), 1617–1631.
- Hecht, J. H., et al. (2009), Imaging of atmospheric gravity waves in the stratosphere and upper mesosphere using satellite and ground-based observations over Australia during the TWIPCE campaign, *J. Geophys. Res.*, **114**(D18123), doi:10.1029/2008JD011259.
- Hertzog, A., G. Boccaro, R. A. Vincent, F. Vial, and P. Cocquerez (2008), Estimation of gravity wave momentum flux and phase speeds from quasi-Lagrangian stratospheric balloon flights. Part II: Results from the Vorcore campaign in Antarctica, *J. Atmos. Sci.*, **65**, 3056–3070.
- Hoffmann, L., and M. J. Alexander (2009), Retrieval of stratospheric temperatures from Atmospheric Infrared Sounder radiance measurements for gravity wave studies, *J. Geophys. Res.*, **114**(D07105), doi:10.1029/2008JD011241.
- Hoffmann, L., and M. J. Alexander (2010), Occurrence frequency of convective gravity waves during the North American thunderstorm season, *J. Geophys. Res.*, **115**(D20111), doi:10.1029/2010JD014401.
- Holton, J. R. (1982), The role of gravity wave induced drag and diffusion on the momentum budget of the mesosphere, *J. Atmos. Sci.*, **39**(4), 791–799.
- Holton, J. R. (1983), The influence of gravity wave breaking on the general circulation of the middle atmosphere, *J. Atmos. Sci.*, **40**(10), 2497–2507.
- Jiang, J. H., D. L. Wu, and S. D. Eckermann (2002), Upper Atmosphere Research Satellite (UARS) MLS observation of mountain waves over the Andes, *J. Geophys. Res.*, **107**(D20), doi:10.1029/2002JD002091.
- Jiang, J. H., B. Wang, K. Goya, K. Hocke, S. D. Eckermann, J. Ma, D. L. Wu, and W. J. Read (2004), Geographical distribution and interseasonal variability of tropical deep convection: UARS MLS observations and analyses, *J. Geophys. Res.*, **109**(D03111), doi:10.1029/2003JD003756.
- Jiang, J. H., S. D. Eckermann, D. L. Wu, K. Hocke, B. Wang, J. Ma, and Y. Zhang (2005), Seasonal variation of gravity wave sources from satellite observation, *Adv. Space Res.*, **35**(11), 1925–1932.
- Jiang, J. H., S. D. Eckermann, D. L. Wu, and D. Y. Wang (2006), Interannual variation of gravity waves in the Arctic and Antarctic winter middle atmosphere, *Adv. Space Res.*, **38**(11), 2418–2423.
- Kalnay, E., et al. (1996), The NCEP/NCAR 40-year reanalysis project, *Bull. Amer. Meteorol. Soc.*, **77**(3), 437–471.
- Kazimirovsky, E. S., and A. D. Danilov (1997), The total ozone content and orography, *Adv. Space Res.*, **20**(6), 1265–1268.
- Kim, S., H. Chun, and D. L. Wu (2009), A study on stratospheric gravity waves generated by Typhoon Ewiniar: Numerical simulations and satellite observations, *J. Geophys. Res.*, **114**(D22104), doi:10.1029/2009JD011971.
- Kuester, M. A., M. J. Alexander, and E. A. Ray (2008), A model study of gravity waves over hurricane Humberto (2001), *J. Atmos. Sci.*, **65**(10), 3231–3246.
- Lambert, A., M. L. Santee, D. L. Wu, and J. H. Chae (2012), A-train CALIOP and MLS observations of early winter Antarctic polar stratospheric clouds and nitric acid in 2008, *Atmos. Chem. Phys.*, **12**(6), 2899–2931, doi:10.5194/acp-12-2899-2012.
- Limpasuvan, V., D. L. Wu, M. J. Alexander, M. Xue, M. Hu, S. Pawson, and J. R. Perkins (2007), Stratospheric gravity wave simulation over Greenland during 24 January 2005, *J. Geophys. Res.*, **112**(D10115), doi:10.1029/2006JD007823.
- Lindzen, R. S. (1981), Turbulence and stress due to gravity wave and tidal breakdown, *J. Geophys. Res.*, **86**, 9707–9714.
- Llamedo, P., A. de la Torre, P. Alexander, D. Luna, T. Schmidt, and J. Wickert (2009), A gravity wave analysis near to the Andes Range from GPS radio occultation data and mesoscale numerical simulations: Two case studies, *Adv. Space Res.*, **44**(4), 494–500.
- Magalhaes, J. M., I. B. Araújo, J. C. B. da Silva, R. H. J. Grimshaw, K. Davis, and J. Pineda (2011), Atmospheric gravity waves in the Red Sea: a new hotspot, *Nonlin. Proc. Geophys.*, **18**(1), 71–79.
- McDonald, A. J., S. E. George, and R. M. Woollands (2009), Can gravity waves significantly impact PSC occurrence in the Antarctic?, *Atmos. Chem. Phys.*, **9**(22), 8825–8840.
- McLandress, C., M. J. Alexander, and D. L. Wu (2000), Microwave Limb Sounder observations of gravity waves in the stratosphere: A climatology and interpretation, *J. Geophys. Res.*, **105**(D9), 11,947–11,967.
- Nastrom, G. D., and D. C. Fritts (1992), Sources of mesoscale variability of gravity waves. Part I: topographic excitation, *J. Atmos. Sci.*, **49**(2), 101–110.
- Parkinson, C. L. (2003), Aqua: an Earth-observing satellite mission to examine water and other climate variables, in *IEEE Trans. Geosci. Remote Sens.*, vol. **41**, pp. 173–183.
- Pfister, L., W. Starr, R. Craig, M. Loewenstein, and M. Legg (1986), Small-scale motions observed by aircraft in the tropical lower stratosphere: Evidence for mixing and its relationship to large-scale flows, *J. Atmos. Sci.*, **43**(24), 3210–3225.
- Plougonven, R., A. Hertzog, and H. Teitelbaum (2008), Observations and simulations of a large-amplitude mountain wave breaking over the Antarctic Peninsula, *J. Geophys. Res.*, **113**(D16113), doi:10.1029/2007JD009739.
- Press, W. H., S. A. Teukolsky, W. T. Vetterling, and B. P. Flannery (2002), *Numerical Recipes in C, The Art of Scientific Computing*, vol. 1, 2. ed., Cambridge University Press: Cambridge, UK.
- Preusse, P., S. D. Eckermann, and M. Ern (2008), Transparency of the atmosphere to short horizontal wavelength gravity waves, *J. Geophys. Res.*, **113**(D24), doi:10.1029/2007JD009682.
- Preusse, P., S. Schroeder, L. Hoffmann, M. Ern, F. Friedl-Vallon, J. Ungermann, H. Oelhaf, H. Fischer, and M. Riese (2009), New perspectives on gravity wave remote sensing by spaceborne infrared limb imaging, *Atmos. Meas. Tech.*, **2**, 299–311.
- Romps, D. M., and Z. Kuang (2009), Overshooting convection in tropical cyclones, *Geophys. Res. Lett.*, **36**(9), doi:10.1029/2009GL037396.
- Sassen, K., Z. Wang, and D. Liu (2009), Cirrus clouds and deep convection in the tropics: Insights from CALIPSO and CloudSat, *J. Geophys. Res.*, **114**(D00H06), doi:10.1029/2009JD011916.
- Smith, R. B. (1985), On severe downslope winds, *J. Atmos. Sci.*, **42**(23), 2597–2603.
- Tsuda, T., Y. Murayama, H. Wiryosumarto, S. W. B. Harijono, and S. Kato (1994), Radiosonde observations of equatorial atmosphere dynamics over Indonesia. 2. characteristics of gravity waves, *J. Geophys. Res.*, **99**(D5), 10,507–10,516.
- Vadas, S. L., D. C. Fritts, and M. J. Alexander (2003), Mechanism for the generation of secondary waves in wave breaking regions, *J. Atmos. Sci.*, **60**, 194–214.
- Vadas, S. L., et al. (2009), Convection: the likely source of the medium-scale gravity waves observed in the OH airglow layer near Brasilia, Brazil, during the SpreadFEx campaign, *Annales Geophysicae*, **27**, 231–259.
- Vadas, S. L., J. Yue, and T. Nakamura (2012), Mesospheric concentric gravity waves generated by multiple convective storms over the North American Great Plain, *J. Geophys. Res.*, doi:10.1029/2011JD017025, in press.

- Vincent, R. A., and M. J. Alexander (2000), Gravity waves in the tropical lower stratosphere: An observational study of seasonal and interannual variability, *J. Geophys. Res.*, *105*(D14), 17,971–17,982.
- Vincent, R. A., A. Hertzog, G. Boccara, and F. Vial (2007), Quasi-Lagrangian superpressure balloon measurements of gravity-wave momentum fluxes in the polar stratosphere of both hemispheres, *Geophys. Res. Lett.*, *34*(L19804), doi:10.1029/2007GL031072.
- Wu, D. L. (2004), Mesoscale gravity wave variances from AMSU-A radiances, *Geophys. Res. Lett.*, *31*(L12114), doi:10.1029/2004GL019562.
- Wu, D. L., and J. H. Jiang (2002), MLS observations of atmospheric gravity waves over Antarctica, *J. Geophys. Res.*, *107*(4773), doi:10.1029/2002JD002390.
- Wu, D. L., and F. Zhang (2004), A study of mesoscale gravity waves over the North Atlantic with satellite observations and a mesoscale model, *J. Geophys. Res.*, *109*(D22104), doi:10.1029/2004JD005090.
- Wu, D. L., P. Preusse, S. D. Eckermann, J. H. Jiang, M. de la Torre Juarez, L. Coy, B. Lawrence, and D. Y. Wang (2006), Remote sounding of atmospheric gravity waves with satellite limb and nadir techniques, *Adv. Space Res.*, *37*, 2269–2277.
- Yue, J., et al. (2009), Concentric gravity waves in the mesosphere generated by deep convective plumes in the lower atmosphere near Fort Collins, Colorado, *J. Geophys. Res.*, *114*(D06104), doi:10.1029/2008JD011244.